*Networks and Heterogeneous Media*

*Research article*

# Exploring dynamics and pattern formation of a fractional-order three-variable Oregonator model

**Jia Yu Yang**[1], **Yu Lan Wang**[1,*] **and Zhi Yuan Li**[2]

[1] Department of Mathematics, Inner Mongolia University of Technology, Hohhot 010051, China

[2] College of Date Science and Application, Inner Mongolia University of Technology, Hohhot 010080, China

* **Correspondence:** Email: wylnei@163.com.

**Abstract:** In this paper, we investigated the nonlinear dynamics and pattern formation of a fractional-order three-variable Oregonator model. We first performed a linear stability analysis of the model without diffusion, deriving equilibrium points and Jacobian eigenvalues, and verified Matignon's stability conditions. A high-precision numerical scheme was developed, and simulations revealed that even tiny variations in fractional order produce significant changes in long-term trajectories. For the reaction-diffusion model, we analyzed Turing instability under integer-order diffusion and derived the critical wave-number conditions via Routh-Hurwitz criteria. Weakly nonlinear analysis near the Turing threshold yielded coupled amplitude equations whose coefficients predicted stripe, hexagon, and mixed patterns. Extensive two-dimensional numerical experiments confirmed the theoretical predictions: Depending on diffusion coefficients and other parameters, the model evolved into bullseye, spiral, labyrinthine, or spot-stripe mixtures.

**Keywords:** fractional Oregonator model; Grünwald–Letnikov derivative; turing instability; spatiotemporal patterns; weakly nonlinear analysis

## 1. Introduction

The Oregonator model is the mathematical dynamic that describes the Field–Körös–Noyes mechanics of the famous Belousov–Zhabotinsky reaction. As the classic theoretical framework for the Belousov-Zhabotinsky reaction, the Oregonator model has been widely studied for its chaotic dynamics [1–4]. Due to the fact that fractional-order differential equations can more accurately describe the dynamic characteristics of complex systems, many researchers have devoted themselves to the study of fractional-order models [5–7]. On one hand, fractional calculus [8,9] has demonstrated unique advantages in describing the dynamic behaviors of complex systems [10,11]. For instance, Diethelm et al. [12,13]

conducted a systematic analysis of the theory and numerical methods of fractional differential equations, laying a solid foundation for subsequent research. Li et al. [14,15] further summarized the fractional-order numerical approximation methods, promoting the application of fractional-order models in high-precision simulations. In the reaction-diffusion system, Zhang et al. [16, 17] studied the fractional dynamics and pattern formation of vegetation-water models, the Hastings-Powell model, and the phytoplankton-zooplankton model, demonstrating the wide application of fractional derivatives in ecological models. Moreover, Petráš [18] systematically expounded the modeling and simulation methods of fractional nonlinear systems, providing theoretical support for the construction of the model in this paper.

On the other hand, the research on fractional-order models and fractional-order dynamical systems has been continuously deepening. Fractional-order models have achieved significant progress in various fields due to their ability to effectively capture the memory and hereditary characteristics of complex systems: In chemical reaction kinetics, they are used to describe the glycerol hydrolysis process [19]; in infectious disease modeling, fractional operators are employed to analyze the transmission patterns of multi-stage infections [20]; and in neural networks, related studies involve the passivity of coupled systems [21], the synchronization of bidirectional ring systems [22], and the finite-time control of time-delay memristive networks [23]. Additionally, the solvability of fractional-order boundary value problems [24,25] and the bifurcation analysis of multi-delay neural networks [26] have enriched the theory of system dynamics. Furthermore, there are researchers, such as Du et al., who analyze the stability of time-delay fractional large-scale double-ring neural networks [27]; Wang et al. studied the improvement of fractional-order PD control on the dynamics of integer-order small-world networks [28]; and Li et al. explored the complex dynamics of fractional-delay plankton models [29]. These achievements and works have jointly promoted the development of fractional-order system theory.

In the field of fractional-order Oregonator model research, Yang et al. first extended the classical model and proposed a three-variable Oregonator model, revealing rich pattern formation phenomena within this nonlinear framework [30]. Subsequently, Peng et al. confirmed in the field of pattern dynamics that this model can exhibit Turing patterns under certain parameter conditions [31]. Jia et al. analyzed the model based on Riemann–Liouville fractional derivatives [32]. Studies have shown that the introduction of fractional differential significantly enhances the sensitivity of the system to initial conditions, making the chaotic attractor structure more complex. In recent years, Xu et al. further introduced a fractional-order Oregonator model with time delay [33,34]. Moreover Li et al.'s research indicates that its pattern types include Turing structures and spatiotemporal oscillation patterns, and the formation mechanism is closely related to reaction rates, diffusion coefficients, and control parameters [35].

In this paper, we introduce fractional-order derivatives into the three-variable Oregonator model [36] study the dynamic characteristics of the following fractional-order Oregonator model.

$$
\begin{cases}
D_t^{\alpha_1} F = \dfrac{1}{\epsilon}\left[ F - F^2 - fG\dfrac{F-q}{F+q} - (cF - dH) \right] + D_F \nabla^2 F, \\
D_t^{\alpha_2} G = F - G + D_G \nabla^2 G, \\
D_t^{\alpha_3} H = \dfrac{1}{\delta}(cF - dH) + D_H \nabla^2 H,
\end{cases}
\tag{1.1}
$$

where $F(x,y,t), G(x,y,t)$, and $H(x,y,t)$ represent the biomass of shallow-rooted herbaceous plants,

deep-rooted shrubs, and the moisture content of the shallow soil at time $t$, respectively. $D_F$, $D_G$, and $D_H$ respectively represent the diffusion coefficients in the model. $\nabla^2 F = \frac{\partial^2 F}{\partial x^2} + \frac{\partial^2 F}{\partial y^2}$ is the Laplacian operator. $\alpha_i (i = 1, 2, 3)$ indicates the order of the Grünwald-Letnikov differential fractional derivative, $D_t^{\alpha_1} F, D_t^{\alpha_2} G$, and $D_t^{\alpha_3} H$ denote the Grünwald-Letnikov fractional derivative, and $t$ is the time variable. The meanings of parameters in this model are shown in Table 1.

**Table 1.** Parameter and biological significance in the model.

| Parameter | Ecological significance |
|---|---|
| $\epsilon$ | The time scale of changes in grass biomass |
| $\delta$ | The time scale of soil moisture variation |
| $f$ | The intensity of competition between shrubs and herbaceous plants |
| $q$ | The threshold for the transformation of competition forms |
| $c$ | The rate at which grass consumes water |
| $d$ | The coefficient of natural regeneration rate of water |

The major contributions of this paper are as follows:

(1) Fractional-order extension: First to incorporate independent Grünwald–Letnikov derivatives into the three-variable Oregonator, establishing eigenvalue-based stability criteria that reveal how fractional order modulates chaos and bifurcation thresholds.

(2) High-precision numerical method: Develop and validate a short-memory, high-order Grünwald–Letnikov scheme, enabling reliable long-time simulation of stiff fractional kinetics.

(3) Novel pattern discovery: Predict and observe unreported "bullseye-maze" and multi-layer spiral–stripe mixed Turing patterns whose morphology is jointly dictated by diffusion coefficients and fractional exponents, confirmed through 2-D weakly nonlinear analysis.

This paper is structured as follows: In Section 2, the dynamic behavior of the model under non-diffusive conditions is analyzed; a high-precision Grünwald–Letnikov numerical algorithm is proposed. In Section 3, we explore Turing instability and derive the critical wave-number conditions via Routh-Hurwitz analysis; we perform extensive two-dimensional numerical simulations that verify the theory and exhibit the dynamic evolution of patterns under varying fractional orders, diffusion coefficients, and initial conditions; and several novel patterns are revealed. Section 4 is the conclusion.

## 2. Dynamical behavior of the model without diffusion

### 2.1. Stability analysis

In this section, the stability of model (1.1) without diffusion is analyzed by finding the equilibrium point of the model, the Jacobian matrix, and the characteristic equation. Model (1.1) is changed as follows:

$$\begin{cases} D_t^{\alpha_1} F = \dfrac{1}{\epsilon} \left[ F - F^2 - fG\dfrac{F - q}{F + q} - (cF - dH) \right], \\ D_t^{\alpha_2} G = F - G, \\ D_t^{\alpha_3} H = \dfrac{1}{\delta}(cF - dH). \end{cases} \tag{2.1}$$

Letting

$$f_1 = 0, \ f_2 = 0, \ f_3 = 0, \tag{2.2}$$

where

$$\begin{cases} f_1 = \dfrac{1}{\epsilon}\left[F - F^2 - fG\dfrac{F-q}{F+q} - (cF - dH)\right], \\ f_2 = F - G, \\ f_3 = \dfrac{1}{\delta}(cF - dH). \end{cases} \tag{2.3}$$

We can get the following equilibrium point of model (2.3).

$$E_0\left(0,0,0\right), \quad E_1\left(F_1, G_1, H_1\right), \quad E_2\left(F_2, G_2, H_2\right), \tag{2.4}$$

where

$$F_1 = \frac{-(f+q-1)+\sqrt{(f+q-1)^2+4q(f+1)}}{2}, \quad G_1 = \frac{-(f+q-1)+\sqrt{(f+q-1)^2+4q(f+1)}}{2}, \quad H_1 = \frac{-c(f+q-1)+c\sqrt{(f+q-1)^2+4q(f+1)}}{2d},$$

$$F_2 = \frac{-(f+q-1)-\sqrt{(f+q-1)^2+4q(f+1)}}{2}, \quad G_2 = \frac{-(f+q-1)-\sqrt{(f+q-1)^2+4q(f+1)}}{2}, \quad H_2 = \frac{-c(f+q-1)-c\sqrt{(f+q-1)^2+4q(f+1)}}{2d}.$$

The Jacobian matrix of the model (2.3) at the equilibrium $(F^*, G^*, H^*)$ is

$$J\left(F^*, G^*, H^*\right) = \begin{pmatrix} f_{1F} & f_{1G} & f_{1H} \\ f_{2F} & f_{2G} & f_{2H} \\ f_{3F} & f_{3G} & f_{3H} \end{pmatrix}, \tag{2.5}$$

where

$$f_{1F} = \frac{1}{\epsilon}\left(1 - 2F^* - c - \frac{2qfG^*}{(F^*+q)^2}\right), \quad f_{1G} = -\frac{f(F^*-q)}{\epsilon(F^*+q)}, \quad f_{1H} = \frac{d}{\epsilon},$$

$$f_{2F} = 1, \quad f_{2G} = -1, \quad f_{2H} = 0, \quad f_{3F} = \frac{c}{\delta}, \quad f_{3G} = 0, \quad f_{3H} = -\frac{d}{\delta}.$$

The characteristic equation is

$$\lambda^{\alpha_1+\alpha_2+\alpha_3} + A_1\lambda^{\alpha_1+\alpha_2} + A_2\lambda^{\alpha_1+\alpha_3} + A_3\lambda^{\alpha_2+\alpha_3} + A_4\lambda^{\alpha_1} + A_5\lambda^{\alpha_2} + A_6\lambda^{\alpha_3} + A_7 = 0, \tag{2.6}$$

where

$$A_1 = -f_{3H}, A_2 = -f_{2G}, A_3 = -f_{1F},$$
$$A_4 = f_{2G}f_{3H} - f_{2H}f_{3G} - f_{1G}f_{2F}, A_5 = f_{1F}f_{3H} - f_{1H}f_{3F}, A_6 = f_{1F}f_{2G} - f_{1G}f_{2F},$$
$$A_7 = f_{1F}(f_{2G}f_{3H} - f_{2H}f_{3G}) - f_{1G}(f_{2F}f_{3H} - f_{2H}f_{3F}) + f_{1H}(f_{2F}f_{3G} - f_{2G}f_{3F}).$$

According to the Matignon's conditions, the necessary condition for the stability of the Oregonator model is that all eigenvalues $\lambda$ are satisfied:

$$|arg\left(\lambda\right)| > \frac{\alpha\pi}{2},$$

where $\alpha = \max\{\alpha_i \mid i = 1, 2, 3\}$. If one of the eigenvalues $\lambda$ satisfies $|arg\left(\lambda\right)| = \frac{\alpha\pi}{2}$, then the model shows Turing bifurcation.

Next, we select two sets of parameters and calculate the eigenvalues and argument at the corresponding equilibrium points to conduct the stability analysis. The equilibrium points and corresponding eigenvalues at $(\alpha_1, \alpha_2, \alpha_3) = (1, 1, 1)$, $\epsilon = 0.2, f = 0.2, q = 0.1, d = 2$, and $c = 0.2, \delta = 1.2$ are shown in Table 2.

**Table 2.** Equilibrium point, eigenvalue, and angle at $(\alpha_1, \alpha_2, \alpha_3) = (1, 1, 1)$, $\epsilon = 0.2, f = 0.2, q = 0.1, d = 2, c = 0.2$, and $\delta = 1.2$.

| Equilibrium point | | | Eigenvalues of Jacobian matrix | | | $|Arg(eig(J))|$ | | |
|---|---|---|---|---|---|---|---|---|
| 0 | 0 | 0 | 4.4555 | −1.1222 | −2 | 0 | 3.1416 | 3.1416 |
| −0.1424 | −0.1424 | −0.0142 | 21.0535 | −0.7604 | −1.7206 | 0 | 3.1416 | 3.1416 |
| 0.8424 | 0.8424 | 0.0842 | −1.1779 − 0.3196i | −1.1779 − 0.3196i | −4.9249 | 2.8766 | 2.8766 | 3.1416 |

The eigenvalues at different fractional orders and the equilibrium point $(0.8424, 0.8424, 0.0842)$ are shown in Table 3.

**Table 3.** Eigenvalues and angles at different fractional-order derivatives.

| Fractional order | Eigenvalues of Jacobian matrix | | | $|Arg(eig(J))|$ | | |
|---|---|---|---|---|---|---|
| $(\alpha_1, \alpha_2, \alpha_3) = (1.2, 1.2, 1.2)$ | −0.8684 ± 0.7999i | −3.2699 ± 1.8879i | −1.1269 ± 0.3521i | 2.3972 | 2.6180 | 2.8388 |
| $(\alpha_1, \alpha_2, \alpha_3) = (1.5, 1.5, 1.5)$ | −1.4473 ± 2.5069i | −0.3884 ± 1.0740i | −0.7360 ± 0.8733i | 2.0944 | 1.9178 | 2.2710 |
| $(\alpha_1, \alpha_2, \alpha_3) = (0.555, 1.112, 1.999)$ | −1.0951 ± 0.3967i | −0.0093 ± 1.1713i | | 2.7940 | 1.5787 | |



$(\alpha_1, \alpha_2, \alpha_3) = (1, 1, 1)$     $(\alpha_1, \alpha_2, \alpha_3) = (1.2, 1.2, 1.2)$     $(\alpha_1, \alpha_2, \alpha_3) = (1.5, 1.5, 1.5)$
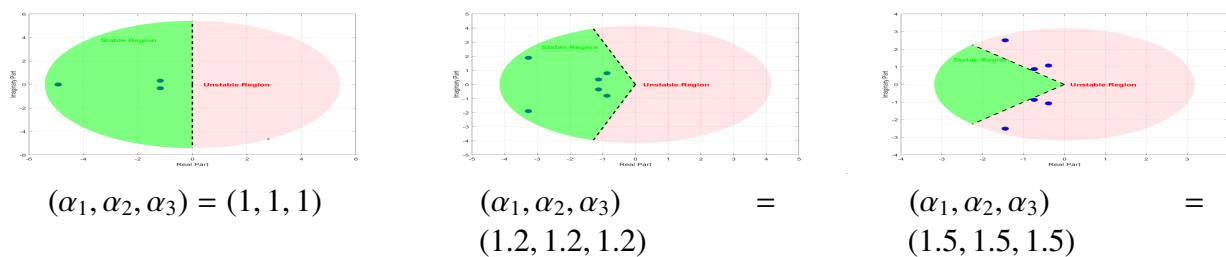
**Figure 1.** The distribution of equilibrium point eigenvalues under different $(\alpha_1, \alpha_2, \alpha_3)$ conditions.

We select the second set of parameters. The equilibrium points and corresponding eigenvalues at $(\alpha_1, \alpha_2, \alpha_3) = (1, 1, 1)$, $\epsilon = 0.1, f = 10, q = 0.3, d = 0.5, c = 1.5$, and $\delta = 0.1$ are shown in Table 4.
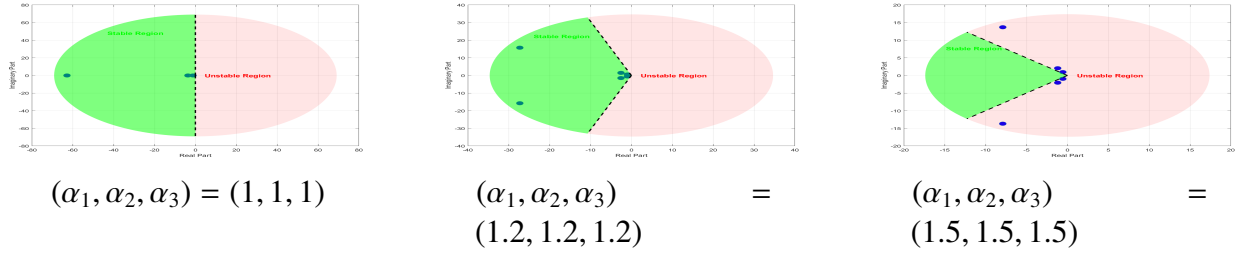
The eigenvalues at different fractional orders and the equilibrium point $(0.3422, 0.3422, 1.0267)$ are shown in Table 5.

**Table 4.** Equilibrium point, eigenvalue, and angle at $(\alpha_1, \alpha_2, \alpha_3) = (1, 1, 1)$, $\epsilon = 0.1, f = 10, q = 0.3, d = 0.5, c = 1.5$, and $\delta = 0.1$.

| Equilibrium Point | | | Eigenvalues of Jacobian matrix | | | $|Arg(eig(J))|$ | | |
|---|---|---|---|---|---|---|---|---|
| 0 | 0 | 0 | 9.5870 | −17.2640 | −3.3230 | 0 | 3.1416 | 3.1416 |
| −9.6422 | −9.6422 | −28.9267 | 194.3050 | −5.3343 | −0.4971 | 0 | 3.1416 | 3.1416 |
| 0.3422 | 0.3422 | 1.0267 | −1.1607 | −3.6486 | −62.8193 | 3.1416 | 3.1416 | 3.1416 |

**Table 5.** Eigenvalues and angles at different fractional-order derivatives.

| Fractional order | Eigenvalues of Jacobian matrix | | | $\lvert Arg(eig(J)) \rvert$ | | |
|---|---|---|---|---|---|---|
| $(\alpha_1, \alpha_2, \alpha_3) = (1.2, 1.2, 1.2)$ | $-2.5466 \pm 1.4703i$ | $-27.2861 \pm 15.7536i$ | $-0.9805 \pm 0.5661i$ | 2.6180 | 2.6180 | 2.6180 |
| $(\alpha_1, \alpha_2, \alpha_3) = (1.5, 1.5, 1.5)$ | $-0.5522 \pm 0.9565i$ | $-1.1850 \pm 2.0525i$ | $-7.9013 \pm 13.6855i$ | 2.0944 | 2.0944 | 2.0944 |
| $(\alpha_1, \alpha_2, \alpha_3) = (1.8, 1.9, 1.65)$ | $-0.7176 + 2.0766i$ | $-0.0848 - 1.0763i$ | $-1.7873 + 9.8615i$ | 1.9035 | 1.6494 | 1.7501 |



$(\alpha_1, \alpha_2, \alpha_3) = (1, 1, 1)$     $(\alpha_1, \alpha_2, \alpha_3) = (1.2, 1.2, 1.2)$     $(\alpha_1, \alpha_2, \alpha_3) = (1.5, 1.5, 1.5)$

**Figure 2.** The distribution of equilibrium point eigenvalues under different $(\alpha_1, \alpha_2, \alpha_3)$ conditions.

Figures 1 and 2 demonstrate the impact of changing the fractional derivative on the stability of the system at the equilibrium point. Among them, the green part represents the stable area, and the pink part represents the unstable area. By comparing these figures, it can be observed that the change in the fractional-order derivative $(\alpha_1, \alpha_2, \alpha_3)$ leads to the variation of the eigenvalues on the complex plane, thereby affecting the stability of the system. As the fractional derivative parameter $\alpha$ increases within a certain range, the distribution of eigenvalues will undergo significant changes, and some eigenvalues may shift from the stable region to the unstable region.

### 2.2. Numerical method

Next, we numerically simulate its dynamic behavior. For this purpose, we introduce a higher-order numerical method.

**Definition 2.1.** *The Grünwald-Letnikov fractional derivative of the $\alpha$-order for a function $f(t)$ is defined as [37]:*

$$D_t^\alpha f(t) = \lim_{h \to 0} \frac{1}{h^\alpha} \sum_{k=0}^{\lfloor (t-t_0)/h \rfloor} (-1)^k \binom{\alpha}{k} f(t - kh),$$

*where the binomial coefficient can be expressed as*

$$(-1)^k \binom{\alpha}{k} = \frac{(-1)^k \Gamma(\alpha + 1)}{\Gamma(k + 1)\Gamma(\alpha - k + 1)},$$

*and $\lfloor \cdot \rfloor$ denotes the floor function, which takes the greatest integer less than or equal to the argument.*

**Definition 2.2.** *The high-precision Grünwald-Letnikov fractional derivative of the $\alpha$-order for a function $f(t)$ is given by [38–41]*

$$D_t^\alpha f(t) = \lim_{h \to 0} \frac{1}{h^\alpha} \sum_{k=0}^{\lfloor (t-t_0)/h \rfloor} \Xi_k^{(\alpha,\omega)} f(t - kh),$$

where $\Xi^{(\alpha,\omega)} = [\Xi_0^{(\alpha,\omega)}, \Xi_1^{(\alpha,\omega)}, \Xi_2^{(\alpha,\omega)}, \cdots]$ *are the Taylor series expansion coefficients of the generating function* $g_\omega^\alpha(z)$.

The high-precision Grünwald-Letnikov fractional calculus can be approximated by:

$$\mathcal{D}_t^\alpha f(t) \approx \frac{1}{h^\alpha} \sum_{k=0}^{[(t-t_0)/h]} \Xi_k^{(\alpha,\omega)} f(t - kh),$$

where the vector $\Xi^{(\alpha,\omega)}$ consists of the coefficients of the Taylor series expansion of the generating function. The Taylor series coefficients $\Xi_k^{(\alpha,\omega)}$ can be computed recursively as:

$$\Xi_k^{(\alpha,\omega)} = \frac{1}{g_0} \sum_{i=1}^{p} g_i \left(1 - i\frac{1+\alpha}{k}\right) \Xi_{k-i}^{(\alpha,\omega)}, \quad \text{if } k = \omega, \omega+1, \omega+2, \cdots.$$

For $m = 1, 2, \cdots, \omega - 1$, the initial coefficients are computed as:

$$\Xi_m^{(\alpha,\omega)} = \frac{1}{g_0} \sum_{i=1}^{m-1} g_i \left(1 - i\frac{1+\alpha}{m}\right) \Xi_{m-i}^{(\alpha,\omega)},$$

with $\Xi_0^{(\alpha,\omega)} = g_0^\alpha$. Where the coefficients $g_k$ can be computed directly from the following equation:

$$\begin{pmatrix} 1 & 1 & 1 & \cdots & 1 \\ 1 & 2 & 3 & \cdots & \omega+1 \\ 1 & 2^2 & 3^2 & \cdots & (\omega+1)^2 \\ \vdots & \vdots & \vdots & \ddots & \vdots \\ 1 & 2^\omega & 3^\omega & \cdots & (\omega+1)^\omega \end{pmatrix} \begin{pmatrix} g_0 \\ g_1 \\ g_2 \\ \vdots \\ g_\omega \end{pmatrix} = - \begin{pmatrix} 0 \\ 1 \\ 2 \\ \vdots \\ \omega \end{pmatrix}.$$

If the number of simulation points is large, the short-memory effect can be utilized to approximate the summation terms, assuming only the most recent $L_0$ samples are retained. Therefore, a high-precision numerical method for the model (2.3) is the following

$$\begin{cases} F_k = h^{\alpha_1} \frac{1}{\epsilon} \left( F_{k-1} - F_{k-1}^2 - f G_{k-1} \frac{F_{k-1}-q}{F_{k-1}+q} - (cF_{k-1} - dH_{k-1}) \right) + F_0 - \sum_{j=1}^{\min(L_0,k)} \Xi_j^{(\alpha,\omega)} \left( F_{k-j} - F_0 \right), \\ G_k = h^{\alpha_2} \left( F_k - G_{k-1} \right) + G_0 - \sum_{j=1}^{\min(L_0,k)} \Xi_j^{(\alpha,\omega)} \left( G_{k-j} - G_0 \right), \\ H_k = h^{\alpha_3} \frac{1}{\delta} \left( cF_k - dH_{k-1} \right) + H_0 - \sum_{j=1}^{\min(L_0,k)} \Xi_j^{(\alpha,\omega)} \left( H_{k-j} - H_0 \right). \end{cases}$$

$$(2.7)$$

## 2.3. Numerical simulation of dynamic behaviors

In this section, in order to verify the effectiveness of this high-precision numerical method, we compare it with the Runge-Kutta (ode45) method and the closed-form solution. In simulations of this section, let parameters $(\epsilon, f, c, q, d, \delta) = (0.01, 0.1, 0.08, 0.1, 2, 2)$ and initial conditions $(F_0, G_0, H_0) = (1, 1, 1)$. We set the time step size $h = 0.01$, and the time is $T = 500$ for the simulations.
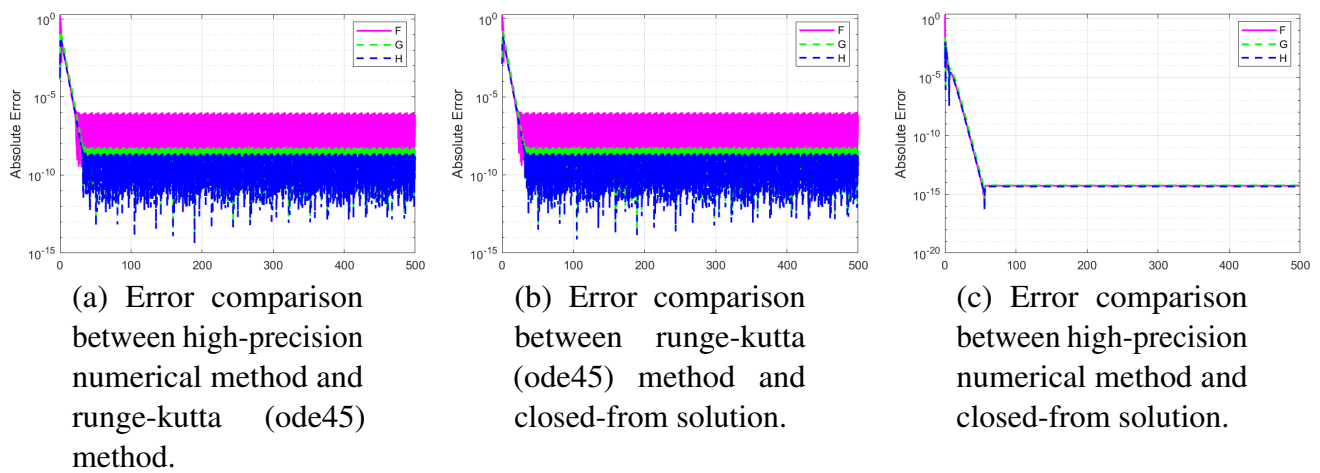
(a) Error comparison between high-precision numerical method and runge-kutta (ode45) method.

(b) Error comparison between runge-kutta (ode45) method and closed-from solution.

(c) Error comparison between high-precision numerical method and closed-from solution.

**Figure 3.** Comparative numerical result of the three methods of the model.

Figure 3 shows the numerical simulations conducted for the problem. Compared with the ode 45 and the closed-from solution, it is found that the simulation results of the high-precision numerical method are in good agreement with the simulation results of other methods, and the accuracy is higher, which verifies the effectiveness of the high-precision numerical method.

We set parameters $\epsilon = 0.2, c = 1.9, f = 0.2, d = 2$, and $\delta = 1.2$, the fractional order value is $(\alpha_1, \alpha_2, \alpha_3) = (0.555, 1.112, 1.999)$, time step size $h = 0.01$, and time $T = 500$. Under these parameters, there is a relatively weak competitive and highly water-renewable ecosystem. The growth of herbaceous plants and shrubs is less restricted by water, and the system is more likely to reach a stable state or undergo periodic oscillations. The simulation results are shown in Figures 4 and 5.
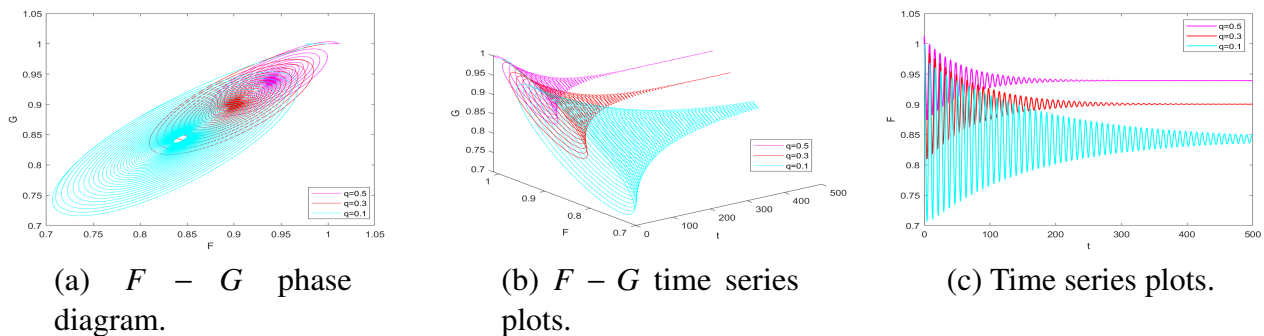


(a) $F - G$ phase diagram.

(b) $F - G$ time series plots.

(c) Time series plots.

**Figure 4.** Comparison of the phase diagrams and time series plots at different parameter values $q$.

Figure 4 shows the comparison of the phase diagrams and time series plots at different parameter values $q$.

Figure 5(a) shows the $F - G$ phase diagram at different fractional-orders. It is found that the trajectories converge to a stable state and perform simple periodic motions. Figure 5(b) shows the $F - G$ time series diagrams under different fractional orders. It is found that at the initial moment, the different fractional order values have a relatively small impact on the system, and the dynamic behavior of the system is relatively consistent. However, as time progresses, the differences in the trajectories under

different orders become more obvious, indicating that the fractional order parameters have a significant influence on the long-term dynamic behavior of the system.
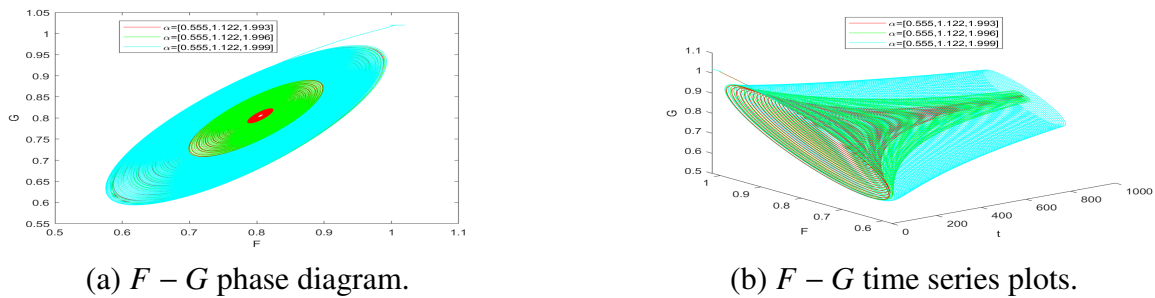


(a) $F - G$ phase diagram.



(b) $F - G$ time series plots.

**Figure 5.** Comparison of dynamical behaviors under different fractional-order derivatives.

Next, we conduct a numerical simulation comparison when the orders of the fractional calculus are different. We set parameters $\epsilon = 0.1, c = 1.5, f = 10, q = 0.3, d = 0.5$, and $\delta = 0.1$, time step size $h = 0.01$, and time $T = 500$. Under these parameters, there is a system with high competition, high water consumption, and a low water reclamation rate. This is prone to cause rapid water depletion, and the system may exhibit chaotic or complex oscillatory behaviors. The simulation results are shown in Figure 6.
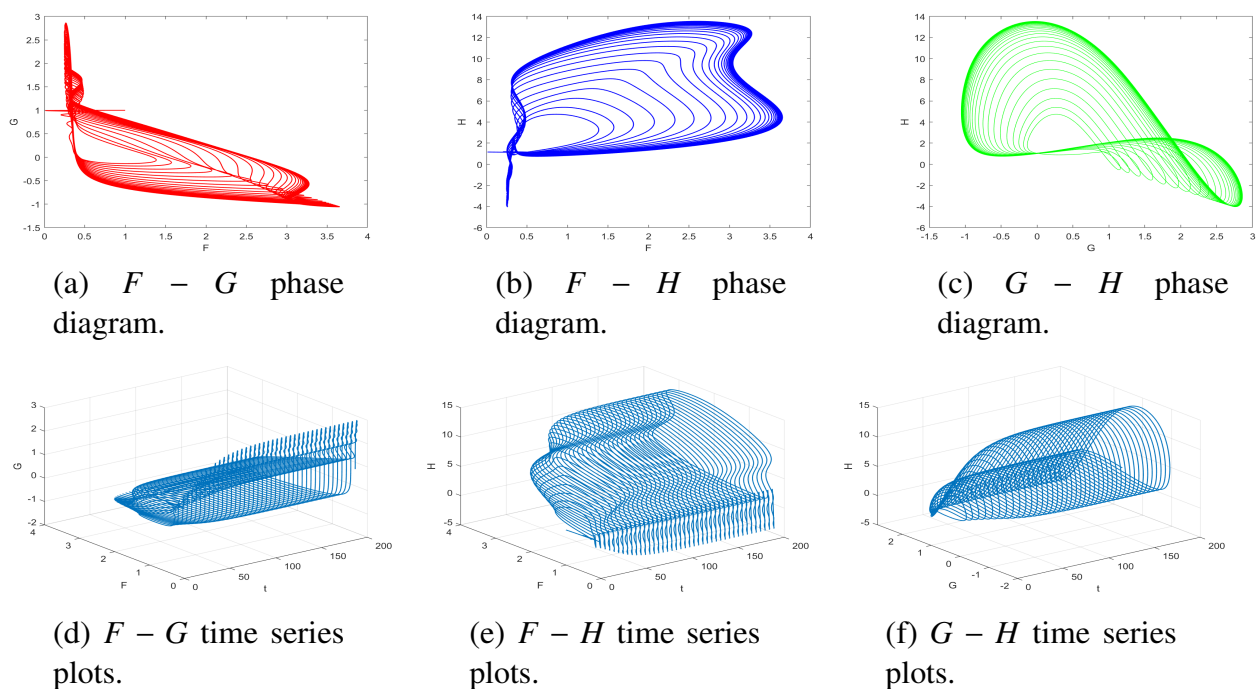


(a) $F - G$ phase diagram.



(b) $F - H$ phase diagram.



(c) $G - H$ phase diagram.



(d) $F - G$ time series plots.



(e) $F - H$ time series plots.



(f) $G - H$ time series plots.

**Figure 6.** Phase diagram and time series plots of the model at $(\alpha_1, \alpha_2, \alpha_3) = (1.8, 1.9, 1.65)$.

Figure 6(a) shows the dynamic relationship between $F$ and $G$. The complex folding and entanglement of the trajectory indicate that the system exhibits non-periodic motion in the phase space. Figure 6(b) shows the dynamic relationship between $F$ and $H$. The trajectory forms complex curves and loops, indicating that the system rapidly switches between states. Figure 6(c) shows the dynamic relationship

between $G$ and $H$, and the trajectory exhibits complex folding and entanglement. Figure 6(d)–(f) present time series graphs. It can be observed that $F, G,$ and $H$ exhibit periodic fluctuations, and then tend to stabilize over time.
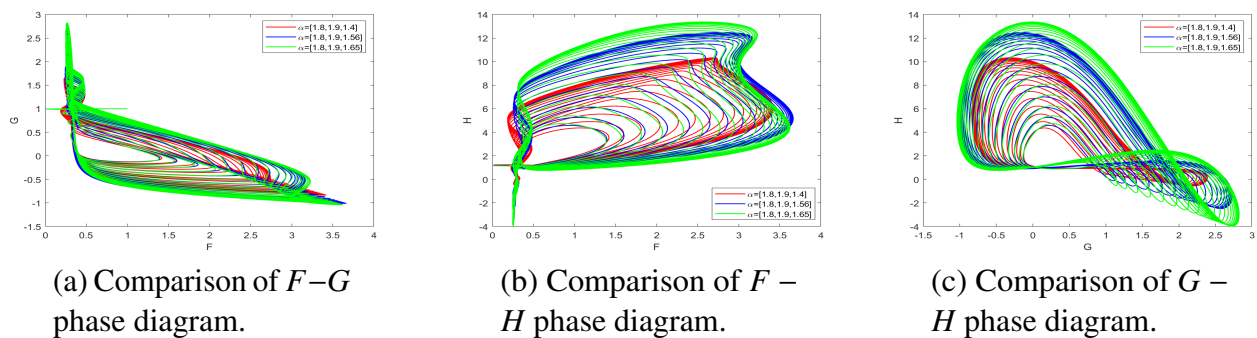


| (a) Comparison of $F-G$ phase diagram. | (b) Comparison of $F-H$ phase diagram. | (c) Comparison of $G-H$ phase diagram. |

**Figure 7.** Comparison of dynamical behaviors at different fractional-order derivatives.

Figure 7 shows that the trajectories with different fractional order values $\alpha$ form a complex attractor structure in the phase space. It is found that a slight change in the fractional order value leads to significant changes in the system behavior.
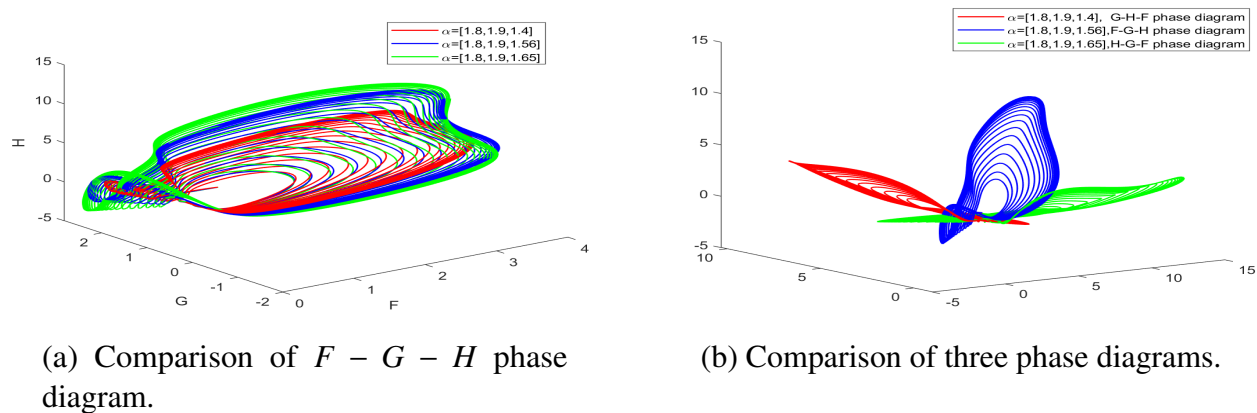


| (a) Comparison of $F-G-H$ phase diagram. | (b) Comparison of three phase diagrams. |

**Figure 8.** Comparison of dynamical behaviors under different fractional-order derivatives.

Figure 8(a) shows a $F-G-H$ phase diagram. It is observed that although the change in the fractional order is relatively small, there are significant differences in the shapes of the trajectories within the phase diagram. This indicates that the system has a high sensitivity to the fractional order. Figure 8(b) shows the comparison of three phase diagrams. When $\alpha = [1.8, 1.9, 1.4]$, it presents the $G-H-F$ phase diagram; when $\alpha = [1.8, 1.9, 1.56]$, it presents the $F-G-H$ phase diagram; and when $\alpha = [1.8, 1.9, 1.65]$, it presents the $H-G-F$ phase diagram. All these demonstrate that even a slight change in the fractional order can have a significant impact on the system. The introduction of fractional derivatives causes the system to exhibit oscillation patterns different from those of integer-order models.

## 3. Dynamical behavior of the model with diffusion

### 3.1. Turing instability

In this section, we discuss the local stability of the model (1.1) at $\alpha_i = 1(i = 1, 2, 3)$. We analyze the Turing instability of the model (1.1) at $\alpha_i = 1(i = 1, 2, 3)$.

$$\begin{cases} \dfrac{\partial F}{\partial t} = \dfrac{1}{\epsilon}\left[F - F^2 - fG\dfrac{F - q}{F + q} - (cF - dH)\right] + D_F\nabla^2 F, \\ \dfrac{\partial G}{\partial t} = F - G + D_G\nabla^2 G, \\ \dfrac{\partial H}{\partial t} = \dfrac{1}{\delta}(cF - dH) + D_H\nabla^2 H. \end{cases} \tag{3.1}$$

Introducing a small disturbance, we get the following:

$$F = F^* + \tilde{F}, \quad G = G^* + \tilde{G}, \quad H = H^* + \tilde{H}. \tag{3.2}$$

By substituting these perturbations into the model (3.1) and ignoring the higher order terms, we get a system:

$$\begin{aligned} \dfrac{\partial \tilde{F}}{\partial t} &= \dfrac{1}{\epsilon}\left[\tilde{F} - \tilde{F}^2 - f\tilde{G}\dfrac{\tilde{F} - q}{\tilde{F} + q} - (c\tilde{F} - d\tilde{H})\right] + D_F\nabla^2 \tilde{F}, \\ \dfrac{\partial \tilde{G}}{\partial t} &= \tilde{F} - \tilde{G} + D_G\nabla^2 \tilde{G}, \\ \dfrac{\partial \tilde{H}}{\partial t} &= \dfrac{1}{\delta}(c\tilde{F} - d\tilde{H}) + D_H\nabla^2 \tilde{H}. \end{aligned} \tag{3.3}$$

The equation can be written in matrix form:

$$\frac{\partial}{\partial t}\begin{pmatrix} \tilde{F} \\ \tilde{G} \\ \tilde{H} \end{pmatrix} = \mathbf{J}\begin{pmatrix} \tilde{F} \\ \tilde{G} \\ \tilde{H} \end{pmatrix} + \mathbf{D}\nabla^2\begin{pmatrix} \tilde{F} \\ \tilde{G} \\ \tilde{H} \end{pmatrix}, \tag{3.4}$$

where $J$ is the Jacobian matrix about $E^*$ and $D = \text{diag}(D_F, D_G, D_H)$ is the diffusion coefficient matrix. By expanding the perturbation variable in Fourier space and substituting $\tilde{F} = c_1 e^{\lambda t + ikx}$, $\tilde{G} = c_1 e^{\lambda t + ikx}$, $\tilde{H} = c_1 e^{\lambda t + ikx}$ into the perturbation equation (3.4), the characteristic equation is:

$$\lambda\begin{pmatrix} c_1 \\ c_2 \\ c_3 \end{pmatrix} = \begin{pmatrix} \frac{1}{\epsilon}\left(1 - 2F^* - c - \frac{2qfG^*}{(F^*+q)^2}\right) - D_F k^2 & -\frac{f(F^*-q)}{\epsilon(F^*+q)} & \frac{d}{\epsilon} \\ 1 & -1 - D_G k^2 & 0 \\ \frac{c}{\delta} & 0 & -\frac{d}{\delta} - D_H k^2 \end{pmatrix}\begin{pmatrix} c_1 \\ c_2 \\ c_3 \end{pmatrix}, \tag{3.5}$$

where, $\lambda_k$ is wavelength and $\lambda_{kx}$, $\lambda_{ky}$ are components of wave number $k$ in the $x$ and $y$ directions, respectively, given by the relation $k^2 = k_x^2 + k_y^2$. We solve the characteristic equation (3.5) to get

$$\lambda_k^3 + I_1\left(k^2\right)\lambda_k^2 + I_2\left(k^2\right)\lambda_k + I_3\left(k^2\right) = 0, \tag{3.6}$$

where

$$I_1(k^2) = (D_F + D_G + D_H)k^2 + C_2,$$

$$I_2(k^2) = (D_F D_G + D_G D_H + D_F D_H)k^4 - (f_{1F}(D_G + D_H) + f_{2G}(D_F + D_H) + f_{3H}(D_F + D_G))k^2 + C_1,$$

$$I_3(k^2) = D_F D_G D_H k^6 - (f_{1F}D_G D_H + f_{2G}D_F D_H + f_{3H}D_F D_G)k^4$$
$$+ (D_F(f_{2G}f_{3H} - f_{2H}f_{3G}) + D_H(f_{1F}f_{2G} - f_{1G}f_{2F}) + D_G f_{1F}f_{3H})k^2 + C_0,$$

where, $C_2 = -(f_{1F} + f_{2G} + f_{3H})$, $C_1 = -(f_{1F}f_{2G} + f_{1F}f_{3H} + f_{2G}f_{3H} - f_{1G}f_{2F} - f_{1H}f_{3F} - f_{2H}f_{3G})$,
$C_0 = f_{1F}f_{2H}f_{3G} + f_{1G}f_{2F}f_{3H} + f_{1H}f_{2G}f_{3F} - f_{1F}f_{2G}f_{3H} - f_{1G}f_{2H}f_{3F} - f_{1H}f_{2F}f_{3G}$.

$$I_1\left(k^2\right) I_2\left(k^2\right) - I_3\left(k^2\right) = \rho_0 + \rho_1 k^2 + \rho_2 k^4 + \rho_3 k^6, \tag{3.7}$$

where

$$\rho_0 = C_1 C_2 - C_0,$$
$$\rho_1 = C_1(D_F + D_G + D_H) + D_F(f_{2H}f_{3G} - f_{2G}f_{3H} - C_2(f_{2G} + f_{3H}))$$
$$- D_N(C_2(f_{1F} + f_{3H}) + f_{1F}f_{3H}) + D_P(f_{1G}f_{2F} - C_2(f_{1F} + f_{2G}) - f_{1F}f_{2G}),$$
$$\rho_2 = C_2(D_G D_H + D_F(D_G + D_H)) + D_G D_H f_{1F} + D_F D_H f_{2G} + D_F D_G f_{3H}$$
$$- (D_F + D_G + D_H) \times (D_F(f_{2G} + f_{3H}) + D_G(f_{1F} + f_{3H}) + D_H(f_{1F} + f_{2G})),$$
$$\rho_3 = (D_F + D_G)(D_F + D_H)(D_G + D_H).$$

According to the Routh-Hurwitz criterion [42], model (3.1) is unstable if it satisfies any of the following conditions.

$$I_2\left(k^2\right) < 0, \quad I_3\left(k^2\right) < 0, \quad I_1\left(k^2\right) I_2\left(k^2\right) - I_3\left(k^2\right) < 0.$$

(1) $I_2\left(k^2\right) < 0$. Let us suppose that $m = k^2$, and we get:

$$I_2(m) = q_1 m^2 + q_2 m + q_3, \tag{3.8}$$

where

$$q_1 = D_F D_G + D_G D_H + D_F D_H,$$
$$q_2 = (D_G + D_H) + f_{2G}(D_F + D_H) + f_{3H}(D_F + D_G)),$$
$$q_3 = C_1,$$

Equation (3.8) has two positive roots:

$$m_{1,2} = \frac{-q_2 \pm \sqrt{q_2^2 - 4q_1 q_3}}{2q_1}.$$

Here, $q_1 > 0$. Turing instability occurs for the range $m_1 < k^2 < m_2$ when $q_2 > 0, q_2^2 - 4q_1 q_3 > 0$.
(2) $I_3\left(k^2\right) < 0$. Similarly, we have

$$I_3(m) = \beta_1 m^3 + \beta_2 m^2 + \beta_3 m + \beta_4,$$

where

$$\beta_1 = D_F D_G D_H,$$

$$\beta_2 = -\left(f_{1F}D_GD_H + f_{2G}D_FD_H + f_{3H}D_FD_G\right),$$
$$\beta_3 = D_F\left(f_{2G}f_{3H} - f_{2H}f_{3G}\right) + D_Gf_{1F}f_{3H} + D_H\left(f_{1F}f_{2G} - f_{1G}f_{2F}\right),$$
$$\beta_4 = C_1.$$

To show that $I_3(m)$ has a minimum, we need to do the following calculations

$$\frac{dI_3}{dm} = 3\beta_1 m^2 + 2\beta_2 m + \beta_3, \quad k_c^2 = \frac{-\beta_2 \pm \sqrt{\beta_2^2 - 3\beta_1\beta_3}}{3\beta_1}.$$

When $\frac{d^2 I_3}{dm^2} = 6\beta_1 m + 2\beta_2 > 0$, we get $\beta_2 < 0, \beta_2^2 - 3\beta_1\beta_3 > 0$. System (3.1) is unstable if

$$I_3\left(k_c^2\right) = \frac{2\beta_2^3 - 9\beta_1\beta_2\beta_3 + 27\beta_1^2\beta_4 - 2\left(\beta_2^2 - 3\beta_1\beta_3\right)^{\frac{3}{2}}}{27\beta_1^3} < 0.$$

(3) Now, for the third condition, we take $I_1\left(k^2\right)I_2\left(k^2\right) - I_3\left(k^2\right) < 0$, for some wave number $k \geq 0$. From Eq (3.7), we get

$$\xi(m) = \rho_3 m^3 + \rho_2 m^2 + \rho_1 m + \rho_0 < 0.$$

In the same way, the Turing instability may occur if we choose $\rho_2 < 0$ and $\rho_1 < 0$ along with the condition

$$\xi\left(k_c^2\right) = \frac{2\rho_2^3 - 9\rho_1\rho_2\rho_3 + 27\rho_0\rho_3^2 - 2\left(\rho_2^2 - 3\rho_1\rho_3\right)^{\frac{3}{2}}}{27\rho_3^3} < 0.$$

**Example 2.1.** The geometric shape or structure of the model system is not the determining factor of Turing instability. What really plays a decisive role is the diffusion coefficient within the system. We adopt the same parameter values as the time model and introduce the diffusion coefficient to study the Turing instability of the spatial model. The values of the parameters and the diffusion coefficient are as follows:

$$\epsilon = 0.2, \quad f = 1.91, \quad q = 0.0015, \quad d = 1, \quad c = 0.2, \quad \delta = 1, \quad D_F = 0.081, \quad D_G = 0.099, \text{ and } D_H = 0.096.$$

From these parameter values, we obtain the equilibrium point and the corresponding variational matrix as follows:

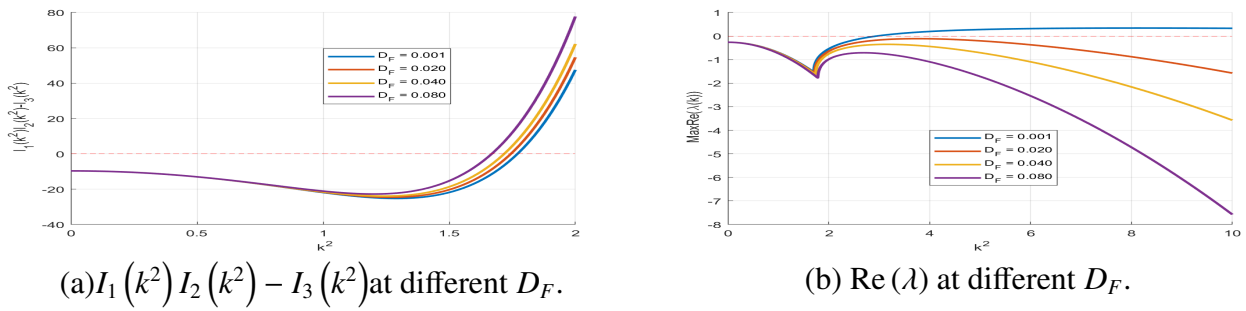$$J(E_1) = \begin{pmatrix} 0.4738 & -4.9762 & 5 \\ 1 & -1 & 0 \\ 0.2 & 0 & -1 \end{pmatrix}.$$

(a) $I_1\left(k^2\right)I_2\left(k^2\right) - I_3\left(k^2\right)$ at different $D_F$.

(b) $\mathrm{Re}\left(\lambda\right)$ at different $D_F$.

**Figure 9.** Variations of $I_1\left(k^2\right)I_2\left(k^2\right) - I_3\left(k^2\right)$ and $\max(Re(k^2))$ with $k^2$.

Figure 9(a) shows that as the diffusion coefficient $D_F$ gradually decreases, the negative space gradually expands, and the critical value of $k^2$ also increases. Figure 9(b) shows the relationship between the wave number $k^2$ and the real part of the eigenvalue $\lambda$ under different diffusion coefficients $D_F$.

Next, we analyze the local stability of model (1.1). The characteristic equation ($J_P$) of the Jacobian matrix is

$$\lambda^{\alpha_1+\alpha_2+\alpha_3} + N_1\lambda^{\alpha_1+\alpha_2} + N_2\lambda^{\alpha_1+\alpha_3} + N_3\lambda^{\alpha_2+\alpha_3} + N_4\lambda^{\alpha_1} + N_5\lambda^{\alpha_2} + N_6\lambda^{\alpha_3} + N_7 = 0, \qquad (3.9)$$

where

$$
\begin{aligned}
N_1 &= -(f_{3H} - D_H k^2), \\
N_2 &= -(f_{2G} - D_G k^2), \\
N_3 &= -(f_{1F} - D_F k^2) + f_{1H}f_{3F}, \\
N_4 &= (f_{2G} - D_G k^2)(f_{3H} - D_H k^2) - f_{2H}f_{3G} - f_{1G}f_{2F}, \\
N_5 &= (f_{1F} - D_F k^2)(f_{3H} - D_H k^2)f_{1H}f_{3F}, \\
N_6 &= \left[(f_{1F} - D_F k^2)(f_{2G} - D_G k^2) - f_{1G}f_{2F} - f_{2H}f_{3G}\right], \\
N_7 &= (f_{1F} - D_F k^2)(f_{2G} - D_G k^2)(f_{3H} - D_H k^2) - f_{2H}f_{3G}(f_{1F} - D_F k^2) \\
&\quad - f_{1H}f_{3F}(f_{2G} - D_G k^2) - f_{1G}f_{2F}(f_{3H} - D_H k^2) - f_{1G}f_{2H}f_{3F} - f_{1H}f_{2F}f_{3G}.
\end{aligned}
$$

According to Matignon's conditions, the necessary condition for the stability of the three-variable Oregonator model is that all eigenvalues $\lambda$ are satisfied:

$$|arg\left(\lambda\right)| > \frac{\alpha\pi}{2},$$

where, $\alpha$ is the highest order of the fractional derivative. If the order $\alpha_i(i = 1, 2, 3)$ is determined, the model will undergo Turing bifurcation when one of the eigenvalues $\lambda$ satisfies $|arg\left(\lambda\right)| = \frac{\alpha\pi}{2}$.

Particularly, when $\alpha_1 = \alpha_2 = \alpha_3 = \alpha$, the characteristic equation (3.9) can be transformed into

$$\lambda^{3\alpha} + (N_1 + N_2 + N_3)\lambda^{2\alpha} + (N_4 + N_5 + N_6)\lambda^{\alpha} + N_7 = 0,$$

at this case, it can be converted into a polynomial equation through variable substitution $s = \lambda^{\alpha}$:

$$s^3 + M_1 s^2 + M_2 s + M_3 = 0,$$

where, $M_1 = (N_1 + N_2 + N_3)$, $M_2 = (N_3 + N_4 + N_5)$, $M_3 = N_7$. The stability can be judged in combination with the Routh-Hurwitz criterion.

## 3.2. Weakly nonlinear analysis

In this section, we adopt a multi-time-scale standard method [43–45] to drive the coefficients of the amplitude equation in the Oregonator model. We apply weak nonlinear analysis to calculate the amplitude equation near the Turing instability threshold $D_F = D_F^c$.

$$f_{1F} = \frac{1}{\epsilon}\left(1 - 2F^* - c - \frac{2qfG^*}{(F^* + q)^2}\right), f_{1G} = -\frac{f(F^* - q)}{\epsilon(F^* + q)}, f_{1H} = \frac{d}{\epsilon},$$

$$f_{1FF} = -\left(\frac{2G^*f(F^* - q)}{(F^* + q)^3} - \frac{2G^*f}{(F^* + q)^2} + 2\right)\frac{1}{\epsilon},$$

$$f_{1FFF} = -\left(\frac{6G^*f}{(F^* + q)^3} - \frac{6G^*f(F^* - q)}{(F^* + q)^4}\right)\frac{1}{\epsilon}, f_{1FG} = -\left(\frac{f}{F^* + q} - \frac{f(F^* - q)}{(F^* + q)^2}\right)\frac{1}{\epsilon},$$

$$f_{1FFG} = \left(\frac{2f}{(F^* + q)^2} - \frac{2f(F^* - q)}{(F^* + q)^3}\right)\frac{1}{\epsilon},$$

$$f_{1GG} = f_{1HH} = f_{1GH} = f_{1FH} = f_{1GGG} = f_{1HHH} = f_{1FHH} = f_{1GGH} = f_{1GHH} = f_{1FGH} = 0,$$

$$f_{2F} = 1, f_{2G} = -1, f_{2H} = f_{2FF} = f_{2FFF} = f_{2GG} = f_{2GGG} = f_{2HH} = f_{2HHH} = f_{2FH} = f_{2FG} = 0,$$

$$f_{2GH} = f_{2FFG} = f_{2FGG} = f_{2FFH} = f_{2FHH} = f_{2GGH} = f_{2GHH} = f_{2FGH} = 0,$$

$$f_{3F} = \frac{c}{\delta}, f_{3G} = 0, f_{3H} = -\frac{d}{\delta}, f_{3FF} = 0, f_{3FFF} = 0, f_{3GG} = 0, f_{3GGG} = 0, f_{3HH} = 0, f_{3HHH} = 0,$$

$$f_{3FH} = f_{3FG} = f_{3GH} = f_{3FFG} = f_{3FGG} = f_{3FFH} = f_{3FHH} = f_{3GGH} = f_{3GHH} = f_{3FGH} = 0.$$

Let $\mathbf{U} = (F, G, H)^T$ and the linearized form of model (3.1) at equilibrium $E^* = (F^*, G^*, H^*)$ be written as follows:

$$\frac{\partial U}{\partial t} = LU + N_1 + N_2, \tag{3.10}$$

where

$$\mathbf{L} = \begin{pmatrix} f_{1F} + D_F\nabla^2 & f_{1G} & f_{1H} \\ f_{2F} & f_{2G} + D_G\nabla^2 & f_{2H} \\ f_{3F} & f_{3G} & f_{3H} + D_H\nabla^2 \end{pmatrix}, \tag{3.11}$$

$$N_1 = \left(\frac{2qG^*f}{(F^* + q)^3\epsilon} - \frac{1}{\epsilon}\right)F^2 - \frac{2qfFG}{(F^* + q)^2\epsilon} + d\left(\frac{1}{\epsilon} - \frac{1}{\delta}\right)FH, \tag{3.12}$$

$$N_2 = \frac{1}{6}\left(-\frac{12qG^*f}{(F^* + q)^4}\frac{F^3}{\epsilon} + \frac{12qf}{(F^* + q)^3}\frac{F^2G}{\epsilon} - \frac{6qf}{(F^* + q)^2}\frac{FG^2}{\epsilon} + \frac{3dF^2H}{\epsilon} + \frac{6dFH^2}{\epsilon} + \frac{cF^3}{\epsilon} - \frac{dH^3}{\delta}\right). \tag{3.13}$$

The linear operator $L$ can be decomposed as follows

$$L = L^cU + (D_F - D_F^c)M, \tag{3.14}$$

where

$$\mathbf{L}^c = \begin{pmatrix} f_{1F} + D_F^c\nabla^2 & f_{1G} & f_{1H} \\ f_{2F} & f_{2G} + D_G\nabla^2 & f_{2H} \\ f_{3F} & f_{3G} & f_{3H} + D_H\nabla^2 \end{pmatrix}, \qquad \mathbf{M} = \begin{pmatrix} \nabla^2 & 0 & 0 \\ 0 & 0 & 0 \\ 0 & 0 & 0 \end{pmatrix}.$$

According to the small parameter $\varepsilon$, variable $U$ and the nonlinear term $N$ are expanded as follows:

$$\mathbf{U} = \varepsilon \mathbf{U}_1 + \varepsilon^2 \mathbf{U}_2 + \varepsilon^3 \mathbf{U}_3 + o(\varepsilon^3). \tag{3.15}$$

Considering only the behavior of the control parameter near the bifurcation point, then the control parameter $D_F$ can be expanded as:

$$D_F - D_F^c = \varepsilon D_F^{(1)} + \varepsilon^2 D_F^{(2)} + \varepsilon^3 D_F^{(3)} + o(\varepsilon^3). \tag{3.16}$$

We divide the time scale of the system into independent $T_0 = t, T_1 = \varepsilon t, T_2 = \varepsilon^2 t$, and, $T_3 = \varepsilon^3 t$. Therefore, the time derivative with respect to $t$ can be expressed as follows:

$$\frac{\partial}{\partial t} = \varepsilon \frac{\partial}{\partial T_1} + \varepsilon^2 \frac{\partial}{\partial T_2} + \varepsilon^3 \frac{\partial}{\partial T_3} + o(\varepsilon^3). \tag{3.17}$$

By inserting Eqs (3.15) − (3.17) into Eq (3.14), we can get the various orders of $\varepsilon$ such as

$$L^c \begin{pmatrix} F_1 \\ G_1 \\ H_1 \end{pmatrix} = 0, \tag{3.18}$$

$$L^c \begin{pmatrix} F_2 \\ G_2 \\ H_2 \end{pmatrix} = \frac{\partial}{\partial T_1} \begin{pmatrix} F_1 \\ G_1 \\ H_1 \end{pmatrix} - D_F^{(1)} M \begin{pmatrix} F_1 \\ G_1 \\ H_1 \end{pmatrix} - h_2, \tag{3.19}$$

$$L^c \begin{pmatrix} F_3 \\ G_3 \\ H_3 \end{pmatrix} = \frac{\partial}{\partial T_1} \begin{pmatrix} F_2 \\ G_2 \\ H_2 \end{pmatrix} + \frac{\partial}{\partial T_2} \begin{pmatrix} F_1 \\ G_1 \\ H_1 \end{pmatrix} - D_F^{(2)} M \begin{pmatrix} F_1 \\ G_1 \\ H_1 \end{pmatrix} - D_F^{(1)} M \begin{pmatrix} F_2 \\ G_2 \\ H_2 \end{pmatrix} - h_3, \tag{3.20}$$

where

$$h_2 = \left( \frac{2qG^*f}{(F^* + q)^3 \epsilon} - \frac{1}{\epsilon} \right) F_1^2 - \frac{2qfF_1 G_1}{(F^* + q)^2 \epsilon} + d \left( \frac{1}{\epsilon} - \frac{1}{\delta} \right) F_1 H_1,$$

$$h_3 = \frac{1}{2} \left[ \left( \frac{4qG^*f}{(F^* + q)^3} - 2 \right) \frac{F_1 F_2}{\epsilon} - \frac{2qf(F_1 G_2 + F_2 G_1)}{(F^* + q)^2 \epsilon} + d \left( \frac{1}{\epsilon} - \frac{1}{\delta} \right) (F_1 H_2 + F_2 H_1) \right]$$
$$+ \frac{1}{6} \left[ - \frac{12qG^*fF_1^3}{(F^* + q)^4 \epsilon} + \frac{12qfF_1^2 G_1}{(F^* + q)^3 \epsilon} - \frac{6qfF_1 G_1^2}{(F^* + q)^2 \epsilon} + \frac{3dF_1^2 H_1}{\epsilon} + \frac{6dF_1 H_1^2}{\epsilon} + \frac{cF_1^3}{\delta} - \frac{dH_1^3}{\delta} \right].$$

Since $L^c$ is defined as the linear operator of the model at the Turing bifurcation threshold $D_F = D_F^c$, the solution of Eq (3.18) can be expressed in the following form.

$$\begin{pmatrix} F_1 \\ G_1 \\ H_1 \end{pmatrix} = \begin{pmatrix} \varphi_1 \\ \varphi_2 \\ 1 \end{pmatrix} \left( \sum_{j=1}^{3} W_j \exp(ik_j r) + c.c. \right), \tag{3.21}$$

where, $\varphi_1 = -\frac{f_{1G}(D_H k_c^2 - f_{3H})}{f_{3G}(f_{1F} - D_F k_c^2)}$, $\varphi_2 = \frac{D_H k_c^2 - f_{3H}}{f_{3G}}$, and $|k_j| = k_c$, $W_j$ represents the amplitude of $\exp(ik_j r)$, and *c.c.* is the complex conjugate of this form.

To ensure that Eq (3.19) has non-trivial solutions, the vector function on the right side of the equation must be orthogonal to the zero eigenvector of operator $L^{c+}$ and the zero eigenvector of the adjoint operator $L^c$. Therefore, $L^{c+}$ is defined as the zero eigenvector of the operator as

$$\begin{pmatrix} 1 \\ \xi_1 \\ \xi_2 \end{pmatrix} \exp(-ik_j \cdot \mathbf{r}) + \text{c.c.}, \tag{3.22}$$

where $\xi_1 = -\frac{D_F k_c^2 - f_{1F}}{f_{2F}}$, $\xi_2 = -\frac{f_{2H}(D_F k_c^2 - f_{1F})}{f_{2F}(f_{3H} - D_H k_c^2)}$, orthogonal conditions as

$$\begin{pmatrix} 1 & \xi_1 & \xi_2 \end{pmatrix} \begin{pmatrix} F_x^j \\ F_y^j \\ F_z^j \end{pmatrix} = 0,$$

where $F_x^j$, $F_y^j$, and $F_z^j$ are defined as the coefficients corresponding to $\exp(ik_j r)$ into terms of $F_x$, $F_y$, and $F_z$. Substituting Eq (3.21) into Eq (3.19) and comparing the coefficients of $\exp(ik_j r)$, we have

$$\begin{pmatrix} F_x^1 \\ F_y^1 \\ F_z^1 \end{pmatrix} = \begin{pmatrix} \xi_1 \\ \xi_2 \\ 1 \end{pmatrix} \frac{\partial W_1}{\partial t_1} + \begin{pmatrix} m_1 D_F^c k^2 \\ 0 \\ 0 \end{pmatrix} W_1 - \begin{pmatrix} Q_{1N} \\ Q_{1G} \\ Q_{1H} \end{pmatrix} \bar{W}_2 \bar{W}_3,$$

where

$$Q_{1N} = \frac{2d}{\epsilon} \varphi_1 - \frac{2f(F^* - q)}{\epsilon(F^* + q)^2} \varphi_1 \varphi_2 - \left( \frac{2G^* f(F^* - q)}{\epsilon(F^* + q)^3} - \frac{2G^* f}{\epsilon(F^* + q)^2} + \frac{2}{\epsilon} \right) \varphi_1^2,$$

$$Q_{1G} = 0, Q_{1Z} = -\frac{2d}{\delta} \varphi_1.$$

According to the Fredholm solubility conditions [46], we get

$$\begin{cases} (\varphi_1 + \varphi_2 \xi_1 + \xi_2) \frac{\partial W_1}{\partial T_1} = -D_F^{(1)} \xi_2 k_c^2 W_1 + (Q_{1N} + \xi_1 Q_{1T} + \xi_2 Q_{1Z}) W_2 \bar{W}_3, \\ (\varphi_1 + \varphi_2 \xi_1 + \xi_2) \frac{\partial W_2}{\partial T_1} = -D_F^{(1)} \xi_2 k_c^2 W_2 + (Q_{1N} + \xi_1 Q_{1T} + \xi_2 Q_{1Z}) \bar{W}_1 W_3, \\ (\varphi_1 + \varphi_2 \xi_1 + \xi_2) \frac{\partial W_3}{\partial T_1} = -D_F^{(1)} \xi_2 k_c^2 W_3 + (Q_{1N} + \xi_1 Q_{1T} + \xi_2 Q_{1Z}) \bar{W}_1 \bar{W}_2. \end{cases}$$

Then, we introduce higher order perturbations. We solve Eq (3.19) to get

$$\begin{pmatrix} F_2 \\ G_2 \\ H_2 \end{pmatrix} = \begin{pmatrix} X_{00} \\ Y_{00} \\ Z_{00} \end{pmatrix} + \sum_{j=1}^{3} \begin{pmatrix} X_j \\ Y_j \\ Z_j \end{pmatrix} \exp(ik_j r) + \sum_{j=1}^{3} \begin{pmatrix} X_{jj} \\ Y_{jj} \\ Z_{jj} \end{pmatrix} \exp(i2k_j r) + \begin{pmatrix} X_{12} \\ Y_{12} \\ Z_{12} \end{pmatrix} \exp(i(k_1 - k_2)r)$$

$$+ \begin{pmatrix} X_{23} \\ Y_{23} \\ Z_{23} \end{pmatrix} \exp(i(k_2 - k_3)r) + \begin{pmatrix} X_{31} \\ Y_{31} \\ Z_{31} \end{pmatrix} \exp(i(k_3 - k_1)r) + \text{c.c.} \tag{3.23}$$

Substituting Eq (3.23) into Eq (3.19) and collecting the coefficients of $\exp(0)$, $\exp(ik_jr)$, $\exp(2ik_jr)$, and $\exp(i(k_j - k_l)r)$, we have

$$\begin{pmatrix} X_{00} \\ Y_{00} \\ Z_{00} \end{pmatrix} = \begin{pmatrix} f_{1F} & f_{1G} & f_{1H} \\ f_{2F} & f_{2G} & f_{2H} \\ f_{3F} & f_{3G} & f_{3H} \end{pmatrix}^{-1} \begin{pmatrix} Q_{1F} \\ Q_{1G} \\ Q_{1H} \end{pmatrix} \left(|W_1|^2 + |W_2|^2 + |W_3|^2\right) = \begin{pmatrix} Z_{xx0} \\ Z_{yy0} \\ Z_{zz0} \end{pmatrix} \left(|W_1|^2 + |W_2|^2 + |W_3|^2\right),$$

$X_j = \varphi_1 Z_j, Y_j = \varphi_2 Z_j, j = 1, 2, 3,$

$$\begin{pmatrix} X_{11} \\ Y_{11} \\ Z_{11} \end{pmatrix} = -\frac{1}{2}\begin{pmatrix} f_{1F} - 4k_c^2 & f_{1G} & f_{1H} \\ f_{2F} & f_{2G} - 4k_c^2 & f_{2H} \\ f_{3F} & f_{3G} & f_{3H} - 4k_c^2 \end{pmatrix}^{-1} \begin{pmatrix} Q_{1F} \\ Q_{1G} \\ Q_{1H} \end{pmatrix} W_1^2 = \begin{pmatrix} Z_{xx1} \\ Z_{yy1} \\ Z_{zz1} \end{pmatrix} W_1^2,$$

$$\begin{pmatrix} X_{12} \\ Y_{12} \\ Z_{12} \end{pmatrix} = -\frac{1}{2}\begin{pmatrix} f_{1F} - 3k_c^2 & f_{1G} & f_{1H} \\ f_{2F} & f_{2G} - 3k_c^2 & f_{2H} \\ f_{3F} & f_{3G} & f_{3H} - 3k_c^2 \end{pmatrix}^{-1} \begin{pmatrix} Q_{1F} \\ Q_{1G} \\ Q_{1H} \end{pmatrix} W_1\bar{W}_2 = \begin{pmatrix} Z_{xx2} \\ Z_{yy2} \\ Z_{zz2} \end{pmatrix} W_1\bar{W}_2.$$

Considering coefficients of terms Eq (3.20), and collecting the coefficients of $\exp(ik_1r)$, we get

$$\begin{pmatrix} R_x^1 \\ R_y^1 \\ R_z^1 \end{pmatrix} = \begin{pmatrix} \varphi_1 \\ \varphi_2 \\ 1 \end{pmatrix}\left(\frac{\partial W_1}{\partial T_2} + \frac{\partial Y_1}{\partial T_1}\right) + \begin{pmatrix} D_F^{(2)} & 0 & 0 \\ 0 & 0 & 0 \\ 0 & 0 & 0 \end{pmatrix}\begin{pmatrix} \varphi_1 \\ \varphi_2 \\ 1 \end{pmatrix} W_1 + \begin{pmatrix} D_F^{(1)} & 0 & 0 \\ 0 & 0 & 0 \\ 0 & 0 & 0 \end{pmatrix}\begin{pmatrix} \varphi_1 \\ \varphi_2 \\ 1 \end{pmatrix} Y_1$$

$$- \begin{pmatrix} Q_{1F} \\ Q_{1G} \\ Q_{1H} \end{pmatrix}\left(\bar{W}_2\bar{Y}_3 + \bar{W}_3\bar{Y}_2\right) - \begin{pmatrix} Q_{2F} \\ Q_{2G} \\ Q_{2H} \end{pmatrix}(|W_1|)^2 W_1 - \begin{pmatrix} Q_{3F} \\ Q_{3G} \\ Q_{3H} \end{pmatrix}\left(|W_2|^2 + |W_3|^2\right) W_1,$$

$$Q_{2G} = 0, Q_{2H} = -\frac{d}{\delta}z_{xx0} - \frac{d}{\delta}z_{xx1}, Q_{3G} = 0, Q_{3H} = -\frac{d}{\delta}z_{xx0} - \frac{d}{\delta}z_{xx2},$$

$$Q_{2F} = \frac{d}{\epsilon}z_{xx0} + \frac{d}{\epsilon}z_{xx1} - \frac{f(F^* - q)}{\epsilon(F^* + q)^2}z_{yy0}\varphi_1 - \frac{f(F^* - q)}{\epsilon(F^* + q)^2}z_{yy1}\varphi_1 - \left(\frac{2G^*f(F^* - q)}{\epsilon(F^* + q)^3} - \frac{2G^*f}{\epsilon(F^* + q)^2} + \frac{2}{\epsilon}\right)z_{xx0}\varphi_1$$

$$- \left(\frac{2G^*f(F^* - q)}{\epsilon(F^* + q)^3} - \frac{2G^*f}{\epsilon(F^* + q)^2} + \frac{2}{\epsilon}\right)z_{xx1}\varphi_1 + \frac{1}{2}\left[-\frac{12qG^*f}{\epsilon(F^* + q)^4}\varphi_1^3 + \frac{12qf}{\epsilon(F^* + q)^3}\varphi_1^2\varphi_2 - \frac{6qf}{\epsilon(F^* + q)^2}\varphi_1\varphi_2^2\right],$$

$$Q_{3F} = \frac{d}{\epsilon}z_{xx0} + \frac{d}{\epsilon}z_{xx2} - \frac{f(F^* - q)}{\epsilon(F^* + q)^2}z_{yy0}\varphi_1 - \frac{f(F^* - q)}{\epsilon(F^* + q)^2}z_{yy2}\varphi_1 - \left(\frac{2G^*f(F^* - q)}{\epsilon(F^* + q)^3} - \frac{2G^*f}{\epsilon(F^* + q)^2} + \frac{2}{\epsilon}\right)z_{xx0}\varphi_1$$

$$- \left(\frac{2G^*f(F^* - q)}{\epsilon(F^* + q)^3} - \frac{2G^*f}{\epsilon(F^* + q)^2} + \frac{2}{\epsilon}\right)z_{xx2}\varphi_1 + \left[-\frac{12qG^*f}{\epsilon(F^* + q)^4}\varphi_1^3 + \frac{12qf}{\epsilon(F^* + q)^3}\varphi_1^2\varphi_2 - \frac{6qf}{\epsilon(F^* + q)^2}\varphi_1\varphi_2^2\right].$$

According to the Fredholm solubility condition of Eq (3.20), it can be obtained that

$$(\varphi_1 + \varphi_2\xi_1 + \xi_2)\left(\frac{\partial W_1}{\partial t_2} + \frac{\partial Y_1}{\partial t_1}\right) = -k_c^2\varphi_2\xi_1\left(D_F^{(2)}W_1 + D_F^{(1)}Y_1\right)$$

$$+ (Q_{1F} + \xi_1Q_{1G} + \xi_2Q_{1H})\left(\bar{W}_2\bar{Y}_3 + \bar{W}_3\bar{Y}_2\right)$$

$$+ (Q_{2F} + \xi_1Q_{2G} + \xi_2Q_{2H})|W_1|^2 W_1$$

$$+ (Q_{3F} + s_1Q_{3G} + s_2Q_{3H})\left(|W_2|^2 + |W_3|^2\right) W_1.$$

The other two equations can be obtained through the transformation of the subscript of W and Y. Moreover, the amplitude of $A_j$ can be expanded as follows

$$\frac{\partial A_j}{\partial t} = \varepsilon \frac{\partial A_j}{\partial T_1} + \varepsilon^2 \frac{\partial A_j}{\partial T_2} + o(\varepsilon^2). \tag{3.24}$$

Based on the above results, we can get the equation about $A_j$

$$\begin{cases} \tau \frac{\partial A_1}{\partial t} = \mu A_1 + h \bar{A}_2 \bar{A}_3 - \left( \gamma_1 |A_1|^2 + \gamma_2 \left( |A_2|^2 + |A_3|^2 \right) \right) A_1, \\ \tau \frac{\partial A_2}{\partial t} = \mu A_2 + h \bar{A}_3 \bar{A}_1 - \left( \gamma_1 |A_1|^2 + \gamma_2 \left( |A_2|^2 + |A_3|^2 \right) \right) A_2, \\ \tau \frac{\partial A_3}{\partial t} = \mu A_3 + h \bar{A}_1 \bar{A}_2 - \left( \gamma_1 |A_1|^2 + \gamma_2 \left( |A_2|^2 + |A_3|^2 \right) \right) A_3, \end{cases} \tag{3.25}$$

where

$$\mu = \frac{D_F^c - D_F}{D_F^c}, \tau = \frac{\varphi_1 + \varphi_2 \xi_1 + \xi_2}{D_F^c k_c^2 \varphi_2 \xi_1}, h = \frac{Q_{1F} + \xi_1 Q_{1G} + \xi_2 Q_{1H}}{D_F^c k_c^2 \varphi_2 \xi_1},$$

$$\gamma_1 = -\frac{Q_{2F} + \xi_1 Q_{2G} + \xi_2 Q_{2H}}{D_F^c k_c^2 \varphi_2 \xi_1}, \gamma_2 = -\frac{Q_{3F} + \xi_1 Q_{3G} + \xi_2 Q_{3H}}{D_F^c k_c^2 \varphi_2 \xi_1}.$$

The amplitude equation can be decomposed into phase angles $\psi_j$ by the mode $\rho_j = |A_j|$. Substituting $A_j = \rho_j exp(i\psi_j)$ in Eq (3.25) and separating the real and imaginary parts, four differential equations with real variables are obtained

$$\begin{cases} \frac{\partial \psi}{\partial t} = -h \frac{\rho_1^2 \rho_2^2 + \rho_1^2 \rho_3^2 + \rho_2^2 \rho_3^2}{\rho_1 \rho_2 \rho_3}, \\ \tau \frac{\partial \rho_1}{\partial t} = \mu \rho_1 + h \rho_2 \rho_3 \cos \psi - \gamma_1 \rho_1^3 - \gamma_2 \left( \rho_2^2 + \rho_3^2 \right) \rho_1, \\ \tau \frac{\partial \rho_2}{\partial t} = \mu \rho_2 + h \rho_1 \rho_3 \cos \psi - \gamma_1 \rho_2^3 - \gamma_2 \left( \rho_1^2 + \rho_3^2 \right) \rho_2, \\ \tau \frac{\partial \rho_3}{\partial t} = \mu \rho_3 + h \rho_1 \rho_2 \cos \psi - \gamma_1 \rho_3^3 - \gamma_2 \left( \rho_1^2 + \rho_2^2 \right) \rho_3, \end{cases} \tag{3.26}$$

where $\psi = \psi_1 + \psi_2 + \psi_3$. The dynamical system (3.24) possesses the following:

(1) Stationary state:

$$\rho_1 = \rho_2 = \rho_3 = 0.$$

Stable when $\mu < \mu_2 = 0$, unstable when $\mu > \mu_2 = 0$.

(2) Strip pattern:

$$\rho_1 = \sqrt{\frac{\mu}{\gamma_1}} \neq 0, \quad \rho_2 = \rho_3 = 0.$$

Stable when $\mu > \mu_3 = \frac{h^2 \gamma_1}{(\gamma_2 - \gamma_1)^2}$, unstable when $\mu < \mu_3 = \frac{h^2 \gamma_1}{(\gamma_2 - \gamma_1)^2}$.

(3) Hexagon pattern:

$$\rho_1 = \rho_2 = \rho_3 = \frac{|h| \pm \sqrt{h^2 + 4(\gamma_1 + 2\gamma_2)\mu}}{2(\gamma_1 + 2\gamma_2)}.$$

When $\mu > \mu_1 = -\frac{h^2}{4(\gamma_1 + 2\gamma_2)}$, $\rho^+ = \frac{|h| + \sqrt{h^2 + 4(\gamma_1 + 2\gamma_2)\mu}}{2(\gamma_1 + 2\gamma_2)}$, is stable and $\mu < \mu_4 = \frac{2\gamma_1 + \gamma_2}{(\gamma_2 - \gamma_1)^2} h^2$, $\rho^- = \frac{|h| - \sqrt{h^2 + 4(\gamma_1 + 2\gamma_2)\mu}}{2(\gamma_1 + 2\gamma_2)}$ is always unstable.

(4) Mixed state:

$$\rho_1 = \frac{|h|}{\gamma_2 - \gamma_1}, \quad \rho_2 = \rho_3 = \sqrt{\frac{\mu - \gamma_1 \rho_1^2}{\gamma_1 + \gamma_2}},$$

it is always unstable with $\gamma_1 < \gamma_2$.

## 3.3. Numerical simulation

In this section, we introduce the numerical method. If $0 < \alpha_i < 1(i = 1, 2, 3)$, the time derivative is expressed by formula, and the space derivative is expressed by a formula. If $\alpha_i = 1(i = 1, 2, 3)$, we use the Euler discrete method for numerical simulation in two-dimensional space $\Omega = [0, L_x] \times [0, L_y]$. Choosing $L_x = 1000, L_x = 200$, time step $\Delta t = 0.25$, and space step $\Delta h = 0.89$, we define $F^n_{pq} = F\left(x_p, y_q, n\Delta t\right)$, $G^n_{pq} = G\left(x_p, y_q, n\Delta t\right)$, and $H^n_{pq} = H\left(x_p, y_q, n\Delta t\right)$. Model (3.1) is discretized by the Euler method as follows:

$$
\begin{cases}
\frac{F^{n+1}_{pq} - F^n_{pq}}{\Delta t} = \frac{1}{\epsilon}\left[F^n_{pq} - F^n_{pq}{}^2 - fG^n_{pq}\frac{F^n_{pq} - q}{F^n_{pq} + q} - (cF^n_{pq} - dH^n_{pq})\right] + D_F\nabla^2 F^n_{pq}, \\
\frac{G^{n+1}_{pq} - G^n_{pq}}{\Delta t} = F^n_{pq} - G^n_{pq} + D_G\nabla^2 G^n_{pq}, \\
\frac{H^{n+1}_{pq} - H^n_{pq}}{\Delta t} = \frac{1}{\delta}(cF^n_{pq} - dH^n_{pq}) + D_H\nabla^2 H^n_{pq},
\end{cases}
$$

where

$$
\nabla^2 F_{pq} = \frac{F_{p+1,q+1} + F_{p-1,q-1} + F_{p+1,q-1} + F_{p-1,q+1} + 4\left(F_{p+1,q} + F_{p-1,q} + F_{p,q+1} + F_{p,q-1}\right) - 20M_{pq}}{6h^2},
$$

$$
\nabla^2 G_{pq} = \frac{G_{p+1,q+1} + G_{p-1,q-1} + G_{p+1,q-1} + G_{p-1,q+1} + 4\left(G_{p+1,q} + G_{p-1,q} + G_{p,q+1} + G_{p,q-1}\right) - 20N_{pq}}{6h^2},
$$

$$
\nabla^2 H_{pq} = \frac{H_{p+1,q+1} + H_{p-1,q-1} + H_{p+1,q-1} + H_{p-1,q+1} + 4\left(H_{p+1,q} + H_{p-1,q} + H_{p,q+1} + H_{p,q-1}\right) - 20P_{pq}}{6h^2}.
$$

**Table 6.** The parameter values for the numerical study of model (3.1).

| $\epsilon$ | f | q | d | c | $\delta$ | $D_F$ | $D_G$ | $D_H$ | $D^c_F$ |
|------------|------|--------|------|------|----------|-------|-------|-------|---------|
| 0.2 | 1.91 | 0.0015 | 1 | 0.2 | 1 | 0.081 | 0.099 | 0.96 | 0.0217 |

For the parameter values given in Table 6, we obtain

$E_* = (0.0048, 0.0048, 0.001)$,
$\mu = 0.9988 - 0.0656i, \ \mu_1 = -0.0002 - 0.0125i, \ \mu_2 = 0, \ \mu_3 = 0.0015 + 0.0847i,$ \hfill (3.27)
$\mu_4 = 6.0683, \ \gamma_1 = 121.44 + 6907.7i, \ \gamma_2 = 370.40 + 21069i, \ h = 0.8720 + 49.6002i, \ k = 3.050.$

From the calculation results, it can be seen that $\gamma_2 > \gamma_1$, and a set of mixed structure solutions is obtained, indicating that this data will produce a mixed pattern under these parameter conditions. We select the following initial conditions

$$
\begin{cases}
F(x, y, 0) = F_* (1 + 0.1 (rand - 0.5)), \\
G(x, y, 0) = G_* (1 + 0.1 (rand - 0.5)), \\
H(x, y, 0) = H_* (1 + 0.1 (rand - 0.5)).
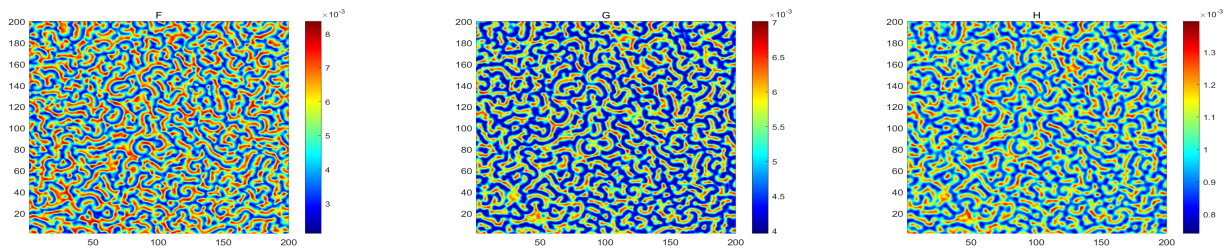\end{cases}
$$

**Figure 10.** The labyrinthine diagram of the model.

The numerical simulation results in Figure 10, show that a mixed pattern consisting of spots and stripes has emerged in the pattern. The simulation results are in agreement with the aforementioned numerical calculations, thereby verifying the correctness of the theory.

We select the following initial conditions for numerical simulations:

$$F(x, y, 0) = \begin{cases} F_*, & x, y \in (80, 120), \\ F_* - 0.001, & other, \end{cases}$$

$$G(x, y, 0) = \begin{cases} G_*, & x, y \in (80, 120), \\ G_* - 0.001, & other, \end{cases}$$

$$H(x, y, 0) = \begin{cases} H_*, & x, y \in (80, 120), \\ H_* - 0.001, & other. \end{cases}$$

When the diffusion coefficient is set to $D_F = 0.081, D_G = 0.099$, and $D_H = 0.96$, we adopt the nine-point difference method for numerical simulations.

**Table 7.** The parameter values for the numerical study of model (3.1).

| $\epsilon$ | f | q | d | c | $\delta$ | $D_F$ | $D_G$ | $D_H$ | $D_F^c$ |
|---|---|---|---|---|---|---|---|---|---|
| 0.2 | 1.91 | 0.0015 | 1 | 0.2 | 1 | 0.081 | 0.099 | 0.96 | 0.0217 |

Based on the parameter values in Table 7, the calculated results are as follows:

$E_* = (0.0048, 0.0048, 0.001),$
$\mu = 0.9988 - 0.0656i, \mu_1 = -0.0002 - 0.0125i, \mu_2 = 0, \mu_3 = 0.0015 + 0.0847i,$      (3.28)
$\mu_4 = 6.0683, \gamma_1 = 121.44 + 6907.7i, \gamma_2 = 370.40 + 21069i, h = 0.8720 + 49.6002i, k = 3.0500.$

Figure 11 is the diffusion plot of parameters $F, G$, and $H$ at different times. Under these parameters, there is a highly competitive and rapidly water-diffusing system, which simulates the influence of water distribution in the real ecosystem on the vegetation pattern. At the beginning, the spot pattern shows a distinct aggregation phenomenon in the central area, forming a pattern similar to the bulldog, with irregular point-like and ring-shaped structures distributed around it. As time goes by, the periodicity of the pattern becomes more obvious, and the ring structure becomes tighter and more regular. The bullseye pattern in the central area forms a complex nested structure with the surrounding ring-shaped structures. Finally, the circular structure becomes more complex, with more layers and details emerging. The circular structures in some areas interweave with each other, forming a pattern similar to a maze.
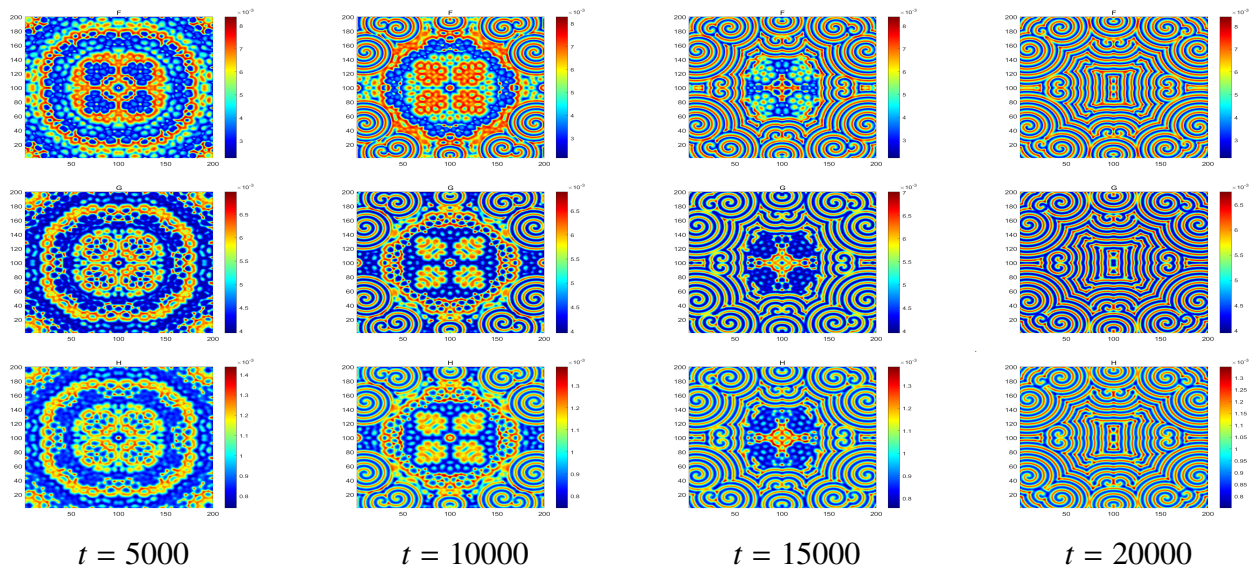
**Figure 11.** Pattern dynamic behavior of $F, G$, and $H$ at different times ($t = 5000, 10000, 15000, 20000$), with diffusion coefficients $D_F = 0.0081, D_G = 0.099$, and $D_H = 0.96$.
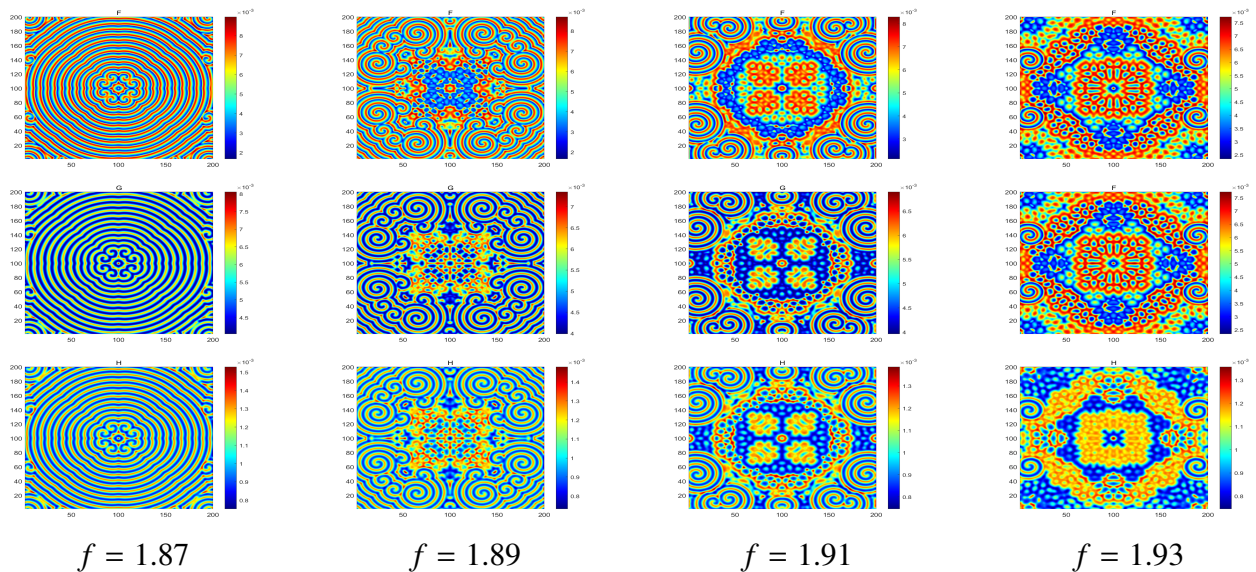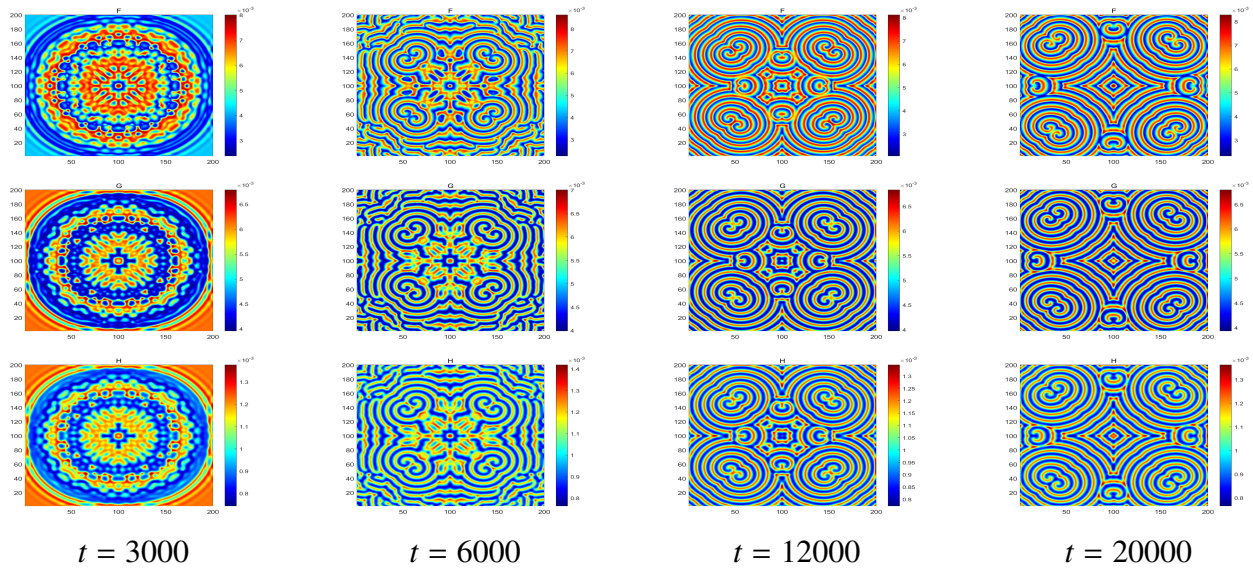


**Figure 12.** Pattern dynamic behavior of $F, G$, and $H$ over $f$ (0.87, 0.89, 0.91, 0.93) at times ($t$=10000), with diffusion coefficients $D_F = 0.0081, D_G = 0.099$, and $D_H = 0.96$.

**Table 8.** The parameter values for the numerical study of model (3.1).

| $\epsilon$ | f | q | d | c | $\delta$ | $D_F$ | $D_G$ | $D_H$ | $D_F^c$ |
|---|---|---|---|---|---|---|---|---|---|
| 0.2 | 1.91 | 0.0015 | 1 | 0.2 | 1 | 0.046 | 0.066 | 0.66 | 0.067 |

Figure 12 shows that as parameter $f$ increases, the structure of the pattern becomes more complex, indicating that the system is highly sensitive to changes in parameter $f$.

When the diffusion coefficient is set to $D_F = 0.046, D_G = 0.066$, and $D_H = 0.66$, we adopt the nine-point difference method for numerical simulations.

Based on the parameter values in Table 8, the calculated results are as follows:

$E_* = (0.0048, 0.0048, 0.001)$,
$\mu = 0.9976 - 0.0404i, \mu_1 = -0.0009 - 0.0147i, \mu_2 = 0, \mu_3 = 0.0035 + 0.0589i$,  (3.29)
$\mu_4 = 3.9968, \gamma_1 = 197.19 + 3343.2i, \gamma_2 = 789.24 + 13381i, h = 2.4840 + 42.1139i, k = 4.0024$.



| $t = 3000$ | $t = 6000$ | $t = 12000$ | $t = 20000$ |

**Figure 13.** Pattern dynamic behavior of $F, G$, and $H$ at different times (t=3000,6000,12000,20000), with diffusion coefficients $D_F = 0.046, D_G = 0.066$, and $D_H = 0.66$.

Figure 13 is the diffusion plot of parameters $F, G$, and $H$ at different times. At the beginning, the pattern presents a ring-shaped structure with central symmetry. As time goes by, the ring-shaped structure becames more complex, and spiral branches begin to appear. These branches are interwoven with each other in space, and the spiral structure further developes, becoming more regular and symmetrical. The spacing of the spirals and the shape of the branches tend to stabilize, forming a neat spiral pattern. Finally, it turns into a complex spiral pattern and reaches a stable and ordered state.

When the diffusion coefficient is set to $D_F = 0.091, D_G = 0.056$, and $D_H = 0.96$. We adopt the nine-point difference method for numerical simulations.

**Table 9.** The parameter values for the numerical study of model (3.1).

| $\epsilon$ | f | q | d | c | $\delta$ | $D_F$ | $D_G$ | $D_H$ | $D_F^c$ |
|---|---|---|---|---|---|---|---|---|---|
| 0.2 | 0.91 | 0.009 | 1 | 0.2 | 2 | 0.091 | 0.056 | 0.96 | 0.1067 |

Based on the parameter values in Table 9, the calculated results are as follows:

$E_* = (0.1777, 0.1777, 0.0355)$,
$\mu = 0.9923 - 0.0809i, \mu_1 = 0.0003 + 0.0031i, \mu_2 = 0, \mu_3 = -0.0028 - 0.0290i$,  (3.30)
$\mu_4 = 7.926, \gamma_1 = -0.1003 - 1.0474i, \gamma_2 = -0.2659 - 2.7785i, h = -0.0276 - 0.2881i, k = 2.6526$.

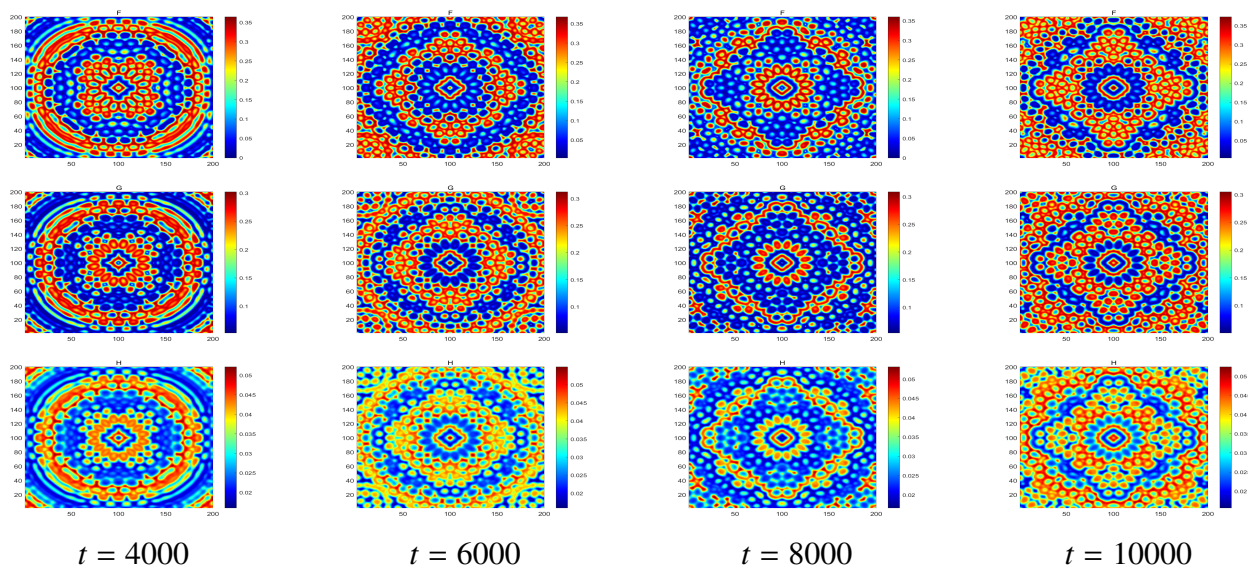|   |   |   |   |
|---|---|---|---|
| $t = 4000$ | $t = 6000$ | $t = 8000$ | $t = 10000$ |

**Figure 14.** Pattern dynamic behavior of $F, G$, and $H$ at different times ($t$=4000,6000,8000,10000), with diffusion coefficients $D_F = 0.091, D_G = 0.056$, and $D_H = 0.96$.

Figure 14 is the diffusion plot of parameters $F, G$, and $H$ at different times. Under these parameters, there is a system where shrubs spread slowly and soil moisture changes slowly. It is prone to form concentric circular layered structures or target-like spot patterns, simulating the periodic distribution of vegetation in space. At the beginning, the pattern presents a concentric circular layered structure. The color in the central part is darker and gradually transitions to a lighter color outward. As time goes by, the concentric circle structure in the central area gradually becomes blurred, replaced by more local spots and stripes, indicating the instability of the system during the process of time evolution. Finally, the spot distribution is more uniform but maintains a certain symmetry and periodicity, indicating that the system has reached a dynamic equilibrium state after a long period of evolution.

## 4. Conclusions

In this paper, we mostly focus on the chaotic dynamic behavior and pattern dynamic behavior of the three-variable Oregonator model. At the beginning of the study, we solved the equilibrium points of the deterministic model and analyzed their stability at those points, thereby laying a theoretical foundation for the subsequent studies. In the field of numerical simulation, for the Oregonator model without diffusion terms, we adopted a high-precision numerical calculation method. The simulation results showed that changes in parameters and the values of fractional derivatives would cause the model to exhibit different dynamic behaviors. This discovery fully indicates that the model is highly sensitive to parameters. Furthermore, the introduction of different fractional order values provides new approaches and possibilities for model optimization. Subsequently, we expanded the research to the three-variable Oregonator model with diffusion terms. To explore the Turing instability of the model, we applied a small perturbation to the model and deeply analyzed its impact. Through this process, we gradually revealed the important role of the diffusion term in the model's dynamic behavior. In the study of pattern formation mechanisms, we derived the coefficients of the amplitude equation through weak

linear analysis. Based on specific parameter values and diffusion coefficients for each group, we used the nine-point difference method to conduct numerical simulations of the model. The simulation results presented a rich variety of pattern forms. Through detailed numerical calculations of these patterns and analysis of their shapes, we successfully verified the correctness of the theoretical derivation and further deepened our understanding of the pattern dynamic behavior of the three-variable Oregonator model. During this process, we discovered a large number of novel and interesting patterns, which greatly expanded our understanding of the diversity of patterns in reaction-diffusion systems.

These research results have broad potential for practical applications. In ecosystem modeling, the model reveals how fractional-order parameters and diffusion coefficients jointly determine the evolution of vegetation spatial patterns, providing a more precise mathematical framework for understanding self-organizing phenomena such as "tiger-striped" vegetation in arid areas. In the fields of materials science and chemical engineering, this model can be applied to describe the formation of microstructures and non-standard dynamic processes on catalytic reaction surfaces. Moreover, the in-depth understanding of the mechanism of system parameter influence provides a theoretical basis for designing control strategies. In future work, we will incorporate the time-delay effect and study the pattern dynamics in non-uniform environments. We will apply this high-precision numerical framework to other more complex fractional-order biochemical systems, further exploring the significant potential of fractional calculus in describing complex phenomena in the real world.

## Use of AI tools declaration

The authors declare we have not used Artificial Intelligence (AI) tools in the creation of this article.

## Acknowledgments

## Conflicts of interest

The authors declare there is no conflict of interest.

## Author contributions

Conceptualization, Methodology, Software, Data, Formal analysis and Funding acquisition, Writing–original draft and writing review and editing: All authors. All authors have read and agreed to the published version of the manuscript.

## References

1. K. Sriram, S. Bernard, Complex dynamics in the Oregonator model with linear delayed feedback, *Chaos*, **18** (2008), 023126. https://doi.org/10.1063/1.2937015

2. H. Mahara, T. Yamaguchi, Y. Morikawa, T. Amemiya, T. Yamamoto, H. Miike, et al., Forced excitations and excitable chaos in the photosensitive Oregonator under periodic sinusoidal perturbations, *Physica D*, **205** (2005), 275–282. https://doi.org/10.1016/j.physd.2005.01.014

3. R. J. Field, R. M. Mazo, N. Manz, Science, serendipity, coincidence, and the Oregonator at the University of Oregon, 1969–1974, *Chaos*, **32** (2022), 052101. https://doi.org/10.1063/5.0087455

4. K. Imaeda, T. Tei, Bifurcation and chaos caused by an external periodic force in the Oregonator of BZ reaction, *J. Phys. Soc. Jpn.*, **55** (1986), 743–752. https://doi.org/10.1143/JPSJ.55.743

5. C. P. Li, Z. Wang, Non-uniform L1/discontinuous Galerkin approximation for the time-fractional convection equation with weak regular solution, *Math. Comput. Simul.*, **182** (2021), 838–857. https://doi.org/10.1016/j.matcom.2020.12.007

6. Z. Y. Li, Y. L. Wang, F. G. Tan, X. H. Wan, H. Yu, J. S. Duan, Solving a class of linear nonlocal boundary value problems using the reproducing kernel, *Appl. Math. Comput.*, **265** (2015), 1098–1105. https://doi.org/10.1016/j.amc.2015.05.117

7. I. Podlubny, *Fractional Differential Equations*, Academic Press, San Diego, 1999.

8. H. Che, Y. L. Wang, Z. Y. Li, Novel patterns in a class of fractional reaction-diffusion models with the Riesz fractional derivative, *Math. Comput. Simul.*, **202** (2022), 149–163. https://doi.org/10.1016/j.matcom.2022.05.037

9. C. Han, Y. L. Wang, Numerical solutions of variable-coefficient fractional-in-space KdV equation with the Caputo fractional derivative, *Fractal Fract.*, **6** (2022), 207. https://doi.org/10.3390/fractalfract6040207

10. X. L. Gao, Z. Y. Li, Y. L. Wang, Chaotic dynamic behavior of a fractional-order financial system with constant inelastic demand, *Int. J. Bifurcation Chaos*, **34** (2024), 2450111. https://doi.org/10.1142/S0218127424501116

11. K. Diethelm, The analysis of fractional differential equations: An application-oriented exposition using differential operators of Caputo type, *Lect. Notes Math.*, 2004.

12. K. Diethelm, N. J. Ford, Analysis of fractional differential equations, *J. Math. Anal. Appl.*, **265** (2002), 229–248. https://doi.org/10.1006/jmaa.2000.7194

13. K. Diethelm, N. J. Ford, A. D. Freed, A predictor-corrector approach for the numerical solution of fractional differential equations, *Nonlinear Dyn.*, **29** (2002), 3–22. https://doi.org/10.1023/A:1016592219341

14. C. P. Li, F. H. Zeng, *Numerical Methods for Fractional Calculus*, Chapman and Hall/CRC, Boca Raton, 2015.

15. C. P. Li, M. Cai, *Theory and Numerical Approximations of Fractional Integrals and Derivatives*, Society for Industrial and Applied Mathematics, Philadelphia, 2019.

16. H. L. Zhang, Y. L. Wang, J. X. Bi, S. H. Bao, Novel pattern dynamics in a vegetation-water reaction-diffusion model, *Math. Comput. Simul.*, **241** (2026), 97–116. https://doi.org/10.1016/j.matcom.2025.09.020

17. S. Zhang, H. L. Zhang, Y. L. Wang, Z. Y. Li, Dynamic properties and numerical simulations of a fractional phytoplankton-zooplankton ecological model, *Networks Heterogen. Media*, **20** (2025), 648–669. https://doi.org/10.3934/nhm.2025028

18. I. Petr'aš, *Fractional-order Nonlinear Systems: Modeling, Analysis and Simulation*, Springer Science & Business Media, Heidelberg, 2011.

19. C. Xu, M. Liao, M. Farman, A. Shehzad, Hydrogenolysis of glycerol by heterogeneous catalysis: A fractional order kinetic model with analysis, *MATCH Commun. Math. Comput. Chem.*, **91** (2024), 635–664. https://doi.org/10.46793/match.91-3.635X

20. C. Xu, M. Farman, Y. Pang, Z. Liu, M. Liao, L. Yao, et al., Mathematical analysis and dynamical transmission of SEIrIsR model with different infection stages by using fractional operator, *Int. J. Biomath.*, **2025** (2025), 2450151. https://doi.org/10.1142/S1793524524501511

21. C. G. Liu, J. L. Wang, Passivity of fractional-order coupled neural networks with multiple state/derivative couplings, *Neurocomputing*, **455** (2021), 379–389. https://doi.org/10.1016/j.neucom.2021.05.050

22. C. Jiang, A. Zada, M. T. Şenel, T. Li, Synchronization of bidirectional N-coupled fractional-order chaotic systems with ring connection based on antisymmetric structure, *Adv. Differ. Equ.*, **2019** (2019), 1–16. https://doi.org/10.1186/s13662-019-2380-1

23. T. Jia, X. Chen, L. He, F. Zhao, J. Qiu, Finite-time synchronization of uncertain fractional-order delayed memristive neural networks via adaptive sliding mode control and its application, *Fractal Fract.*, **6** (2022), 502. https://doi.org/10.3390/fractalfract6090502

24. Y. Zhao, Y. Sun, Z. Liu, Y. Wang, Solvability for boundary value problems of nonlinear fractional differential equations with mixed perturbations of the second type, *AIMS Math.*, **5** (2020), 557–567. https://doi.org/10.3934/math.2020037

25. Z. Liu, Y. Ding, C. Liu, C. Zhao, Existence and uniqueness of solutions for singular fractional differential equation boundary value problem with $p$-Laplacian, *Adv. Differ. Equ.*, **2020** (2020), 83. https://doi.org/10.1186/s13662-019-2482-9

26. R. Xing, M. Xiao, Y. Zhang, J. Qiu, Stability and Hopf bifurcation analysis of an (n+ m)-neuron double-ring neural network model with multiple time delays, *J. Syst. Sci. Complexity*, **35** (2022), 159–178. https://doi.org/10.1007/s11424-021-0108-2

27. X. Du, M. Xiao, J. Qiu, Y. Lu, J. Cao, Stability and dynamics analysis of time-delay fractional-order large-scale dual-loop neural network model with cross-coupling structure, *IEEE Trans. Neural Networks Learn. Syst.*, **36** (2024), 7873–7887. https://doi.org/10.1109/TNNLS.2024.3413366

28. H. Wang, M. Xiao, B. Tao, F. Xu, Z. Wang, C. Huang, et al., Improving dynamics of integer-order small-world network models under fractional-order PD control, *Sci. China Inf. Sci.*, **63** (2020), 112206. https://doi.org/10.1007/s11432-018-9933-6

29. P. Li, R. Gao, C. Xu, Y. Li, A. Akgül, D. Baleanu, Dynamics exploration for a fractional-order delayed zooplankton–phytoplankton system, *Chaos, Solitons Fractals*, **166** (2023), 112975. https://doi.org/10.1016/j.chaos.2022.112975

30. L. Yang, M. Dolnik, A. M. Zhabotinsky, I. R. Epstein, Pattern formation arising from interactions between Turing and wave instabilities, *J. Chem. Phys.*, **117** (2002), 7259–7265. https://doi.org/10.1063/1.1507110

31. R. Peng, F. Sun, Turing pattern of the Oregonator model, *Nonlinear Anal.*, **72** (2010), 2337–2345. https://doi.org/10.1016/j.na.2009.10.034

32. Y. Jia, F. Feng, Y. Zhang, Y. He, Pattern formation induced by subdiffusion in Oregonator model, *J. Hebei Univ. (Nat. Sci. Ed.)*, **37** (2017), 19–25.

33. C. Xu, C. Aouiti, Z. Liu, P. Li, L. Yao, Bifurcation caused by delay in a fractional-order coupled Oregonator model in chemistry, *MATCH Commun. Math. Comput. Chem.*, **88** (2022), 371–396. https://doi.org/10.46793/match.88-2.371X

34. C. Xu, W. Zhang, C. Aouiti, Z. X. Liu, L. Yao, Bifurcation dynamics in a fractional-order Oregonator model including time delay, *MATCH Commun. Math. Comput. Chem.*, **87** (2022), 397–414. https://doi.org/10.46793/match.87-2.397X

35. H. Li, Y. Yao, M. Xiao, Z. Wang, L. Rutkowski, Turing pattern dynamics in a fractional-diffusion Oregonator model under PD control, *Nonlinear Anal. Model. Control*, **30** (2025), 1–21. https://doi.org/10.15388/namc.2025.30.38967

36. F. C. Liu, X. F. Wang, Multi-armed spiral waves in three-component reaction diffusion systems, *J. Hebei Univ. (Nat. Sci. Ed.)*, **29** (2009), 376–380.

37. C. P. Li, F. H. Zeng, *Numerical Methods for Fractional Calculus*, Chapman and Hall/CRC, Boca Raton, 2015.

38. D. Y. Xue, C. N. Zhao, Y. Q. Chen, A modified approximation method of fractional order system, in *Proceedings of IEEE International Conference on Mechatronics and Automation*, (2006), 1043–1048. https://doi.org/10.1109/ICMA.2006.257769

39. D. Y. Xue, L. Bai, Numerical algorithms for Caputo fractional-order differential equations, *Int. J. Control*, **90** (2017), 1201–1211. https://doi.org/10.1080/00207179.2016.1158419

40. D. Y. Xue, *Fractional Calculus and Fractional-Order Control*, Science Press, Beijing, 2018.

41. X. H. Wang, H. L. Zhang, Y. L. Wang, Z. Y. Li, Dynamic properties and numerical simulations of the fractional Hastings-Powell model with the Grünwald-Letnikov differential derivative, *Int. J. Bifurcation Chaos*, **35** (2025), 2550145. https://doi.org/10.1142/S0218127425501457

42. M. Bodson, Explaining the Routh–Hurwitz criterion: A tutorial presentation, *IEEE Control Syst. Mag.*, **40** (2020), 45–51. https://doi.org/10.1109/MCS.2019.2949974

43. Z. Bao, Q. Zhou, Z. Yang, Q. Yang, L. Xu, T. Wu, A multi time-scale and multi energy-type coordinated microgrid scheduling solution—Part I: Model and methodology, *IEEE Trans. Power Syst.*, **30** (2014), 2257–2266. https://doi.org/10.1109/TPWRS.2014.2367127

44. S. Ghorai, S. Poria, Emergent impacts of quadratic mortality on pattern formation in a predator–prey system, *Nonlinear Dyn.*, **87** (2017), 2715–2734. https://doi.org/10.1007/s11071-016-3222-2

45. S. Kumari, R. K. Upadhyay, P. Kumar, V. Rai, Dynamics and patterns of species abundance in ocean: A mathematical modeling study, *Nonlinear Anal. Real World Appl.*, **60** (2021), 103303. https://doi.org/10.1016/j.nonrwa.2021.103303

46. X. L. Gao, H. L. Zhang, X. Y. Li, Research on pattern dynamics of a class of predator-prey model with interval biological coefficients for capture, *AIMS Math.*, **9** (2024), 18506–18527. https://doi.org/10.3934/math.2024901